The Pennsylvania State University

The Graduate School

College of Earth and Mineral Sciences

THE ORINOCO LOW-LEVEL JET

A Dissertation in

Meteorology and Atmospheric Science

by

Jorge Giovanni Jiménez Sánchez

Submitted in Partial Fulfillment
of the Requirements
for the Degree of

Doctor of Philosophy

December 2018

Beneficiario COLFUTURO 2014

The dissertation of Jorge Giovanni Jiménez Sánchez was reviewed and approved* by the following:

Paul Markowski
Professor of Meteorology
Associate Head Graduate Program in Meteorology
Dissertation Advisor
Chair of Committee

George S. Young
Professor of Meteorology

Andrew M. Carleton
Professor of Physical Geography

David J. Stensrud
Professor of Meteorology

*Signatures are on file in the Graduate School

ABSTRACT

The low-level jet over the Orinoco River basin is characterized using finer horizontal, vertical, and temporal resolution than possible in previous studies via dynamical downscaling. The investigation relies on a 5-month-long simulation (November 2013-March 2014) performed with the Weather Research and Forecasting model, with initial and boundary conditions provided by the Global Forecast System analysis. Dynamical downscaling is demonstrated to be an effective method to better resolve the horizontal and vertical characteristics of the Orinoco low-level jet, not only improving its diurnal and austral-summer evolution, the identification and location of low-level jet streaks inside the stream tube, but also in determining the mechanisms leading to its formation.

The Orinoco low-level jet (OLLJ) is found to be a single stream tube over Colombia and Venezuela with wind speeds greater than 8 m s^{-1}, and four distinctive cores varying in height under the influence of sloping terrain. The OLLJ has its maximum monthly mean wind speed (13 m s^{-1}) and largest spatial extent (2100 km × 400 km) in January. The maxima mean wind speeds (13–17 m s^{-1}) in the diurnal cycle occur in the early morning above the nocturnal inversion; wind speeds are a minimum (8–9 m s^{-1}) in the late afternoon when a deep, approximately unstratified boundary layer is present.

The momentum balance analysis performed in a streamwise- and crosswise-rotated coordinate system reveal that the OLLJ is the result of four phenomena acting together to accelerate the wind: a sea-breeze penetration over the Orinoco River delta and Unare River depression, katabatic flow down the Coastal Cordillera, three expansion fans from point wakes in topography, and diurnal variation of turbulent diffusivity. The latter, in contrast to the heavily studied nocturnal low-level jet in the U.S. Great Plains region, plays only a secondary role in OLLJ acceleration. These results suggest that LLJs near the equator may originate from processes other than the inertial oscillation and topographic thermal forcing.

TABLE OF CONTENTS

LIST OF FIGURES

LIST OF TABLES

LIST OF ABBREVIATIONS

AGL	Above ground level
C1–C4	Core 1,2,3, and 4
C_{gc}	Gravity current propagation speed
ENE	East-northeast
ENSO	El Niño-Southern Oscillation
ERA-Interim	European Centre for Medium-Range Weather Forecasts Re-Analysis
FAC	Fuerza Aérea Colombiana
Fr	Froude Number
GFS	Global Forecast System
ITCZ	Intertropical convergence zone
LHS	Left-hand side
LLJ	Low-level jet
LLJS	Low-level jet streak
LST	Local Standard Time
MEI	Multivariate ENSO index
MJO	Madden-Julian Oscillation
MYNN2	Mellor-Yamada-Nakanishi-Niino-Level-2.5 PBL scheme
NET	Near-equatorial trough
NOAH	National Centers for Environmental Prediction, Oregon State University, Air Force Weather Agency, and Hydrologic Research Lab
OLLJ	Orinoco low-level jet
PBL	Planetary boundary layer
PGF	Pressure gradient force
RRTMG	Rapid-Radiative-Transfer-Model for GCMs
SBF	Sea breeze front
SSW	South-southwest
TKE	Turbulent kinetic energy
UTC	Universal time coordinated
WRF	Weather research and forecast model
WRF-ARW	WRF advanced research model

ACKNOWLEDGMENTS

This has been quite a journey! A journey that has taken me out of my comfort zone and has expanded not only my knowledge but the self-consciousness of who I was, who I am, what I am capable of, and who I will be in the near future.

Many, many (many!) people have made this possible. From the academic side, I want to thank the extraordinary professors that I had, Dr. Marcelo Chamecki, Dr. Jerry Harrington, Dr. George Young, and Dr. Raymond Najjar because they believed in me and gave me the inspiration, motivation, tools, and courage to give them back only my best. And because research is not only done by going to class, I want to thank the research group of which I was a part, Dr. Yvette Richardson, Branden Katona, Eli Dennis, Michael Colbert, Dr. Alex Anderson-Frey, and Alicia Klees for the fruitful discussions and informal advice whenever it was needed. Special gratitude to Dr. Valerian Jewtoukoff who guided me patiently at the beginning and left me ready to continue learning by myself; without him, this journey could have taken a couple more years. Finally, I'm grateful to my doctoral committee, Dr. Paul Markowski, Dr. George Young, Dr. David Stensrud, and Dr. Andrew Carleton, whose keen insights and right advice opened my mind to new perspectives and understanding. Thank you, Paul, for being the stupendous advisor you were, for agreeing to work with me, in the project that I had in mind, and let me work at my own pace. All of what you are as a person and professional is reflected in this successful achievement.

From the emotional side, I want to thank my once grad-student colleagues, Dr. Livia Souza Freire Grion, Dr. Liza Diaz, Dr. Bicheng Chen, Jesús Ruiz-Plancarte, Vanessa Monteiro, Paulo Soares, Kelly Nuñez, Dandan Wei, Yuting He, Arkayan Samaddar, Kyle

Elliot, Lee Dunnavan, Scott Loeffler, Robert Nystrom, and Sham Thanekar for providing the academic, logistic, sportive, and friendship support needed to succeed in grad school. I'm also thankful to my dear Colombian and Latino group of friends (too many to name) because you were my extended family afar.

From the spiritual side, thanks to God for opening the right doors so that this opportunity became a reality, and for enlightening my mind in the darkest moments.

From my heart, thanks to my parents and my sister for their continued support from abroad. Life, in so many aspects, continued there, and they were fundamental to keep it going. However, no words can express the immense gratitude I feel to my outstanding beloved wife, Erika Basabe, the one who God gave me as a gift, for believing since the beginning in this crazy idea, for leaving her life on hold to come with me, and for her patience, support, and encouragement when everything looked confused. You deserve this too! And to my daughter Juana, your existence makes mine the happiest!

This research and the whole enriching experience were funded by Colciencias-Colfuturo grants and the Colombian Air Force, where I'm proud to serve. Thanks for the opportunity of letting me grow my country every day.

Chapter 1

Introduction

Colombia, the country I am from, unites the Caribbean Sea, Pacific Ocean, Amazon forest, Llanos savannas, and three branches of the Andes Cordillera in a little more than 1.000.000 km^2. Because of the geographic diversity of the many valleys, plateaus, mountains, and hydrological basins, mesoscale meteorology is a critical factor in determining the regional weather.

As a weather officer in the Colombian Air Force, one of the mesoscale phenomena that lured my attention during daily meteorological analyses was a low-level wind maximum above the flatlands of the Orinoco River basin during the austral summer, herein referred to as the Orinoco low-level jet (OLLJ). It is well-known to aircrews because of its effects on aircraft performance.

According to the International Civil Aviation Organization (ICAO; 2005), LLJs are among the atmospheric phenomena that can cause low-level wind shear; i.e., a localized change in wind speed, direction, or both at low altitudes. The presence of wind shear is relevant to aircraft landings and take offs (Guan and Yong 2002; Kulesa 2002; Golding 2005), because in these phases of flight the aircraft airspeed and height are near critical values, so any lift increase or reduction caused by wind shear produces a new resultant flight path vector (Fig. 1.1). During the approach phase of flight, for instance, this sudden new trajectory destabilizes the aircraft (Bonner 1968), potentially causing them to land short of the runway (Blackadar 1957), or reducing the time pilots have for adjusting the glide path. It is estimated that in cases of strong wind shear, pilots only have 5–15 seconds to correctly react to this hazardous situation (Golding 2005).

The OLLJ poses a risk to aviation at the more than ten regional airports and military bases situated within the basin in Colombia and Venezuela, where more than one million passengers per year are transported (Unidad Administrativa de Aeronáutica Civil 2017). The risk is particularly significant when considering that the road infrastructure in the flatlands is not reliable or dense, and airplanes are the primary transportation means connecting this region to the more populated part of the country.

The OLLJ has been previously identified and characterized using mesoscale simulations (Vernekar et al. 2003; Rife et al. 2010), and a combination of pilot balloons, radiosondes, surface data, and reanalysis (e.g., Douglas et al. 2005; Labar et al. 2005; Torrealba and Amador 2010; Rueda 2015). However, the mechanisms leading to its formation remain unknown and, given the spatial and temporal limitations in observations and numerical model resolutions of the previous studies, the OLLJ characteristics and evolution are unsatisfactory resolved.

The research presented in this dissertation addresses the shortcomings of previous investigations by performing a dynamical downscaling of the large-scale atmospheric conditions provided by the Global Forecast System (GFS) analysis data. In Chapter 2 it will be shown that the finer spatial and temporal resolutions, achieved with the advanced-research version of the Weather Research and Forecasting (WRF) model, improves not only the horizontal and vertical characteristics of the OLLJ but also its diurnal and austral-summer evolution. Chapter 3 examines the dynamical origins of the OLLJ, which differ considerably from those of the U.S. Great Plains nocturnal low-level jet. The latter is attributable to an inertial oscillation and cooling of gently sloped terrain. Finally, a summary and conclusions are presented in Chapter 4.

Figures

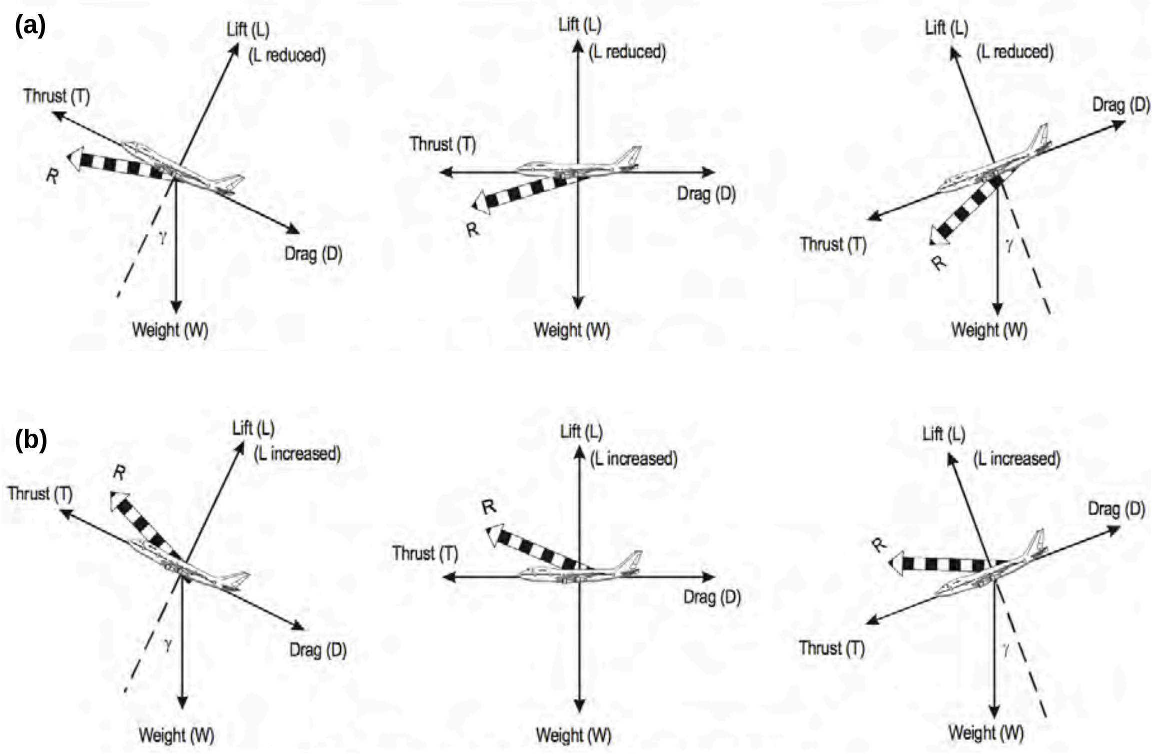

Figure 1.1: Resultant flight path vector (R) due to shear in the horizontal wind during climb, level flight, and descent phases: (a) following airspeed decrease due to decreasing headwind or increasing tailwind, (b) following airspeed increase due to increasing headwind or decreasing tailwind [Adapted from ICAO (2005)].

Chapter 2

Characteristics and Evolution

2.1 Introduction

Low-level jets (LLJs) have been studied for about 80 years in various parts of the world (Blackadar 1957; Bonner 1968; Stensrud 1996; Marengo et al. 2004; Muñoz et al. 2008). Differences arising in the maximum wind speed, altitude, spatial extent, horizontal and vertical shear, and formation mechanisms have precluded a universally accepted definition (Liu et al. 2014). However, in general terms, LLJs refer to relative maxima in vertical profiles of horizontal wind speed (Markowski and Richardson 2010) that are confined to the boundary layer or lower troposphere (below 700 hPa).

LLJs have been the focus of many prior investigations owing to the diversity of their impacts. These include wind energy generation (Storm et al. 2009; Archer et al. 2014), fire weather (Fromm and Servranckx 2003; Petroliagkis et al. 2015), transport of hazardous airborne substances (Banta et al. 2004; Darby et al. 2006), air quality (Banta et al. 1998, 2006), bird migration (Liechti and Schaller 1999), and aviation (Blackadar 1957; International Civil Aviation Organization 2005; Balmez and Ştefan 2014).

As a weather officer of the Colombian Air Force (Fuerza Aérea Colombiana (FAC) in Spanish), I noticed that, during the Austral summer in the flatlands of the Orinoco River basin (Fig. 2.1), a low-level wind maximum is the predominant feature in lower atmospheric analyses and operational model output.

These flatlands, also known as Llanos Savannas (Olson and Dinerstein 2002), describe a wide ellipsoidal arc about 1300 km in length, beginning in the northern Colombian Amazon forest, and ending in the Mesas region adjacent to Delta Amacuro (Venezuela); here the river meets with the Gulf of Paría and the Atlantic Ocean. The Llanos, covering approximately 400,000 km^2, are bounded to the southeast by the Guiana Highlands, to the west by the Eastern Cordillera and the Mérida Cordillera, and to the north by the Coastal Cordillera (Fig. 2.1).

Because the Llanos Savannas are located in northern South America, they are part of the tropics, where abundant moisture content and high temperatures are the distinctive characteristics. As opposed to higher latitudes, the temperature exhibits an ample diurnal variation and reduced seasonality (Hastenrath 1991).

In this part of the continent, the major semi-permanent climatic controls at low levels are the subtropical highs, Intertropical Convergence Zone (ITCZ), and trade winds. The speed and direction of the trade winds depend on the seasonal position of the subtropical highs and the ITCZ.

During the Austral summer, the ITCZ moves to its southernmost position (Walters et al. 1989), while the North Atlantic subtropical high is closest to the equator. The combination of these migrations increases the meridional pressure gradient—producing stronger easterlies than during the winter (Hastenrath 1991; Tim and Bravo de Guenni 2016)— and allows the northeasterly trade winds to reach southern latitudes. Northeasterly trade winds are the main constituent of the aforementioned low-level wind maximum over the Orinoco River flatlands.

This so-called Orinoco low-level jet (OLLJ) has been previously identified using reanalysis products (e.g., Montoya et al. 2001; Rueda 2015), mesoscale simulations (e.g., Vernekar et al. 2003; Rife et al. 2010), and pilot balloons and radiosondes (e.g., Douglas et al. 2005; Labar et al. 2005; Torrealba and Amador 2010). However, because of the broad scope of these previous studies (global or regional), the wide grid spacing of the models used (from 32 km to 111 km), and spatial or temporal limitations in observations (e.g., pilot balloons/radiosondes network) the characteristics and evolution of the OLLJ have been poorly resolved; only partial characterizations over Colombia or Venezuela have been achieved.

Additionally, the distinctive elevations of the Eastern Cordillera (above 3000 m) and Guiana Highlands (around 1500 m), as well as the widths of the Mérida and Coastal cordilleras (approximately 100 km), play an important role in the behavior of the OLLJ and are not properly resolved by today's global models.

The characteristics and evolution of the OLLJ are investigated herein by performing a dynamical downscaling of the large-scale atmospheric conditions provided by the Global Forecast System (GFS) analysis data. A finer spatial and temporal resolution than in the aforementioned studies—more than three times, in most cases—is achieved through the advanced-research version of the Weather Research and Forecasting (WRF) model.

The WRF dynamical downscaling is described in the next section. Section 2.3 analyzes the OLLJ characteristics and its spatial and temporal variability, while results are discussed in Section 2.4. Finally, a summary and conclusions are presented in Section 2.5.

2.2 Dynamical downscaling and model configuration

A way to address the resolution limitations of the global models for regional applications is dynamical downscaling. The purpose of this nested modeling technique is to obtain high-resolution detail over the region of interest, using initial and boundary conditions provided by a coarse-resolution large-scale model (Lo et al. 2008).

High-resolution modeling of the OLLJ is performed with the Advanced Research-WRF model (WRF-ARW) Version 3.4.1 (Skamarock and Klemp 2008), a state-of-the-art atmospheric modeling system designed for both meteorological research and numerical weather prediction. The WRF-ARW is not only developed and studied by a broad community of researchers, but it is also used by FAC to generate the operational weather products distributed to the Colombian military aircrews.

The following physical parameterization schemes and models are used to represent the atmospheric dynamics near and above the surface, where variations in the exchanges of heat, moisture, and momentum affect the OLLJ. The NOAH (National Centers for Environmental Prediction, Oregon State University, Air Force Weather Agency, and Hydrologic Research Lab) land-surface model (Chen and Dudhia 2001) handles the surface energy budget. The Mellor-Yamada-Nakanishi-Niino-Level-2.5 (MYNN2; Nakanishi and Niino 2006) planetary boundary layer (PBL) scheme parameterizes the turbulent mixing within the lower troposphere. The MYNN2 is a local mixing, 1.5-order closure scheme that predicts sub-grid turbulent kinetic energy (TKE) terms. The Kain–Fritsch (Kain 2004) cumulus parameterization scheme is used to parameterize deep convection by mixing the environmental air with convective updrafts and downdrafts to compute the net effect of convection on the model variables. The Rapid-Radiative-Transfer-Model for GCMs (RRTMG) longwave and shortwave radiation schemes (Mlawer et al. 1997; Iacono et al. 2008) account for the radiation components alteration to the total radiative flux caused by clouds, water vapor, and other gases. The Thompson microphysics scheme (Thompson et al. 2008) represents the processes controlling the formation, growth, and fallout of microphysical water species, including ice, snow, and graupel. The WRF model configuration is summarized in Table 2.1.

Dynamical downscaling from November 2013–March 2014 creates regional analyses over northern South America with 9 km horizontal grid spacing and 51 vertical levels (from surface up to 50 hPa), in hourly outputs. The domain is centered at 7ºN and 68.5ºW with dimensions of 407 × 284 grid points, which is equivalent to 3633 km × 2556 km (Fig. 2.1).

The aforementioned five-month period was chosen taking into account the results obtained by Montoya et al. (2001), Vernekar et al. (2003), Douglas et al. (2005), Labar et al. (2005), Torrealba and Amador (2010), and Rueda (2015) showing the presence of the OLLJ mostly during the austral summer, and because the Multivariate El Niño-Southern Oscillation (ENSO) Index (MEI)[1] (Wolter and Timlin 1993) exhibits positive and negative monthly values less than 0.3×10^{-3} standard deviations, indicating that the effect of ENSO on the wind variability is not significant.

Initial and boundary conditions from 1200 UTC 31 October 2013 to 1200 UTC 1 April 2014 were provided by the 0.5º x 0.5º GFS Analysis (Unidata/University Corporation for Atmospheric Research et al. 2003). The GFS Analysis depicts an historical base state of the atmosphere at six-hour intervals (0000, 0600, 1200, and 1800 UTC) based on four separate models (i.e., an atmosphere model, an ocean model, a land/soil model, and a sea ice model), which work together to generate a picture of weather conditions. The boundary conditions were updated every 6 hours and, because frequent reinitialization gives better

---

[1] MEI monitors ENSO based on observations of six main variables over the tropical Pacific: sea-level pressure, zonal and meridional components of the surface wind, sea surface temperature, surface air temperature, and total cloudiness fraction of the sky.

results than continuous simulation runs (Lo et al. 2008), the model was reinitialized every 4 days with a preceding spin-up of 12 hours. This reinitialization procedure means that new initial, and lateral meteorological and surface boundary conditions were provided 12 hours previous to the first day of each 4-day run, but those initial running hours were not considered as part of the long-term run.

2.3 Orinoco low-level jet spatial and temporal variability

2.3.1 Orinoco low-level jet identification

Following the methods established by Ranjha et al. (2013) for identifying coastal LLJs and by Bonner (1968) for identifying the U.S. Great Plains LLJ, the following criteria were used to identify the OLLJ:

- The level of maximum wind is within the lowest 2 km in the vertical;
- The wind speed at the level of maximum wind is at least 40% higher than the wind speed at the surface (i.e., the lowest model level);
- The wind speed above the level of maximum wind decreases by at least 20% within 3 km of the surface.

2.3.2 Structure and spatial variability

To capture the mean horizontal structure of the OLLJ, as well as its height variability, a single representation of the wind field is achieved by averaging the wind velocity vector over time (November 2013–March 2014) and averaging the 950–800-hPa layer afterward (Fig. 2.2a).

The OLLJ, as shown in Fig. 2.2, is a stream tube 2000 km long, 300 km wide, and 2.5 km deep, with mean wind speeds greater than 8 m s^{-1}. This wind speed threshold was chosen to identify the presence of the LLJ because it guarantees that any wind speed of the same or greater magnitude complies with the established filtering criteria. The OLLJ flows westward from 61ºW to 67ºW along 8ºN approximately and then it is deflected equatorward, flowing next to the Cordillera from 8ºN down to the equator. In the last part of its course, around 2ºN and 74ºW, it is slightly deviated eastward and separated from the Eastern Cordillera by the Macarena mountain range.

As the OLLJ flows, the mean height of its axis of maximum wind increases, from 750 m AGL in the entrance region where the wind is mostly zonal (Fig. 2.2d) to 1200 m AGL upon reaching the sloping terrain of the Eastern Cordillera (Fig. 2.2c). It rises to 1500 m AGL in the exit region (Fig. 2.2b), possibly influenced by the underlying elevation of the Macarena mountain range upstream.

Inside this stream tube, there are four low-level jet streaks (LLJSs; i.e., the regions with maximum wind speeds) with mean wind speeds greater than 10 m s^{-1}. The first streak (C1), mainly flowing in zonal direction, is located over the Guanipa Mesa at around 9.5ºN and 64.2ºW. The second streak (C2) is located over the Venezuelan Llanos Savannas (centered around 7.5ºN and 67ºW), next to the northwestern limit of the Guiana Highlands. Along the Eastern Cordillera in Colombia, at 5ºN and 72ºW, is the third streak (C3). The fourth streak (C4) is located over the Colombian Amazon forest at 2ºN and 73.5ºW. The latter three (C2, C3, C4) are directed toward the southwest.

2.3.3 Temporal variability

2.3.3.1 Austral-summer evolution

The horizontal evolution of the OLLJ during the austral summer, shown in Fig. 2.3 (a–b, d–e, g–h), is described through the behavior of the 950–800-hPa-layer mean wind field for each month and the monthly wind-speed anomalies (each monthly mean compared against the five-month mean). A vertical cross-section of the lower troposphere along 5ºN from 66ºW to 74ºW, also shown in Fig. 2.3 (c, f, i), depicts the horizontal and vertical variability of the stream tube under the influence of surrounding sloped terrain (i.e., the Eastern Cordillera to the west and the Guiana Highlands to the east), in the mid-corridor region[2].

November shows the highest negative anomalies in the monthly mean wind speed (Fig. 2.3b), greater than –2 m s^{-1} for most of the Orinoco River basin, meaning that this is the month when the OLLJ is the least intense. However, mean wind speeds greater than 8 m s^{-1} are noticeable from the Orinoco delta down to the equator (Fig. 2.3a), and the OLLJ is already a single structure of 1900 km in length (very close to its average value). The stream tube in the C3 region is 2.5 km deep but only ~250 km wide (Fig. 2.3c).

January is when the OLLJ mean wind speeds are the most intense (~13 m s^{-1}), with positive mean wind speed anomalies greater than 1 m s^{-1} inside the whole stream tube, and even reaching positive values greater than 2 m s^{-1} over the C4 region (Fig. 2.3e). The C4 region, or exit region, has elongated down to its most southerly position at 1ºS, covering a small area of the Ecuadorian and Peruvian Amazon forest (Fig. 2.3d) with a core height of

---

[2] An enhanced visualization of the 3D-structure evolution of the OLLJ during the Austral summer is presented in Figure A1 in appendix A.

1250 m AGL, the lowest of the season (not shown). Also, during January is when the C3 region extends the furthest east, reaching a total width of approximately 400 km with mean winds greater than 12 m s^{-1} present over at least 250 km (Fig. 2.3f).

By March the OLLJ weakens in intensity and reduces in spatial extent; most of the stream tube with mean wind speeds greater than 8 m s^{-1} lies north of 2ºN, and the monthly mean wind speeds in C1, C2 and C3 are mainly around 10 m s^{-1}. The C4 region is small (Fig. 2.3g) but higher than before (not shown), reaching 2000 m AGL, the highest core altitude during the season. The most significant wind speed weakening also occurs in this region, where the monthly anomalies reach –2 m s^{-1} (Fig. 2.3h).

2.3.3.2 Intraseasonal variability

A periodogram-based technique, known as multitaper power spectral density estimation, was used to assess the periodicity of the wind speed and potential temperature in the intraseasonal scale (i.e., days to weeks). This technique uses multiple tapers, or windows, to form independent estimates of the spectral density and reduce the variance of the spectral density estimate (Percival and Walden 1993). The multitaper method overcomes some of the limitations of conventional Fourier analysis related to the assumption that each Fourier coefficient is a reliable representation of the amplitude and relative phase of the corresponding component frequency; an assumption that is not always valid.

The wind speed and potential temperature hourly time series were constructed by averaging a 45 km × 45 km-box centered at 5ºN–72ºW (C3 core) in the 900–850 hPa layer. The normalized spectral power in the resultant periodogram (Fig. 2.4) shows, with a confidence level greater than 99%, that the most significant cycles occur every 12 and 24 hours. No other meaningful periodicity could be identified, in part because the time series is not long enough to assess the influence of extended variabilities.

The strength of these diurnal and semidiurnal signals, in both the wind speed (Fig. 2.4a) and potential temperature (Fig. 2.4b), implies a modulation of the wind via radiative heating, possibly on account of similar oscillations in the atmospheric tide. The atmospheric tide, generated by the daily march of the sun and the absorption of solar radiation by ozone and water vapor (Lindzen and Chapman 1969), exhibits diurnal (24 h), semidiurnal (12 h), and terdiurnal (8 h) pressure variations that reflect in analogous wind and temperature fluctuations (Hastenrath 1991).

2.3.3.3 Diurnal cycle

The diurnal variation of the OLLJ is presented in Fig. 2.5, which shows the 950–800-hPa-layer wind field averaged for the entire period (November 2013–March 2014) in four-hour increments (0000, 0400, 0800, 1200, 1600, and 2000 UTC). Two time zones, UTC–04 and UTC–05, are observed over the region; however, to facilitate the understanding of the physical processes involved in the strengthening or weakening of the OLLJ, UTC–05 will be used to describe its Local Standard Time (LST) behavior. Accordingly, Fig. 2.5 represents the mean wind field at 1900, 2300, 0300, 0700, 1100, and 1500 LST. An enhanced visualization of the 3D-structure evolution of the OLLJ during the day is presented in Figure A2 in appendix A.

As a whole, during the diurnal cycle the OLLJ is the most intense and reaches its greatest spatial extent at 0700 LST (Fig. 2.5d). The four-LLJS regions are noticeable. The

C1-C2 region is the largest with the strongest mean wind speeds (max. of 14 m s^{-1}), whereas C4 is the smallest and weakest (max. of 12 m s^{-1}). The four-LLJS structure remains throughout the day.

As the sun rises and warms up the surface via radiative heating, vigorous turbulent vertical mixing occurs in the boundary layer causing the winds to slow down. At 1500 LST the wind speeds are the least intense, and the OLLJ also exhibits its greatest spatial reduction (Fig. 2.5f). Despite the weakening wind, the stream tube is mostly a single structure, except for the C4 region which lies separated downstream of the former.

Late in the afternoon, with the weakening of radiative heating, the surface layer begins to cool down, and the lower troposphere becomes statically stable impeding the upward propagation of frictionally retarded air, so the air just above this layer becomes frictionless and accelerates.

Because weakening of the radiative heating occurs sooner at the farthest east region than at the most western locations, the low-level air accelerates progressively in the along-stream direction, as shown in Fig. 2.6. The greatest positive wind-speed anomalies (i.e., departure from the 24-h mean) in the entrance region occur near midnight (Fig. 2.6c), whereas in the mid-corridor and exit regions these occur just after sunrise (Fig. 2.6e and 2.6d, respectively). When comparing different locations at the same time (e.g., Fig. 2.6a–2.6c), the geographical differences in wind-speed anomalies are even more evident; while there are already strong positive anomalies occurring in the entrance region, just weak positive anomalies occur in the exit region [i.e., to the east of 74ºW, where the core is located (Fig. 2.2b)].

A better depiction of the intensity of the wind in the lower 5 km of the troposphere is achieved by hourly averaging the wind speed at each vertical level where the OLLJ is present, accordingly to the cross sections P, Q, and R in Fig. 2.2 (b–d). The wind-speed vertical structures obtained at the entrance, mid-corridor and exit region, as well as their diurnal evolution, are given in Fig. 2.7.

The vertical structures of the wind speed portrayed in Fig. 2.7 (c–e) not only support the results about the geographical differences in wind speed peak-time, but also provide information about the height, intensity, and vertical speed shear of the OLLJ. Near midnight in the entrance region (Fig. 2.7c) the maximum mean wind speed is ~15 m s^{-1} at 500 m AGL with an underlying vertical speed shear of 2×10^{-2} s^{-1}. At 0700 LST in the mid-corridor region (Fig. 2.7e) the maximum mean wind speed is ~15 m s^{-1} at 700 m AGL with an underlying vertical speed shear of 1.5×10^{-2} s^{-1}, whereas in the exit region (Fig. 2.7d) the maximum mean wind speed is ~12 m s^{-1} at 1250 m AGL with an underlying vertical speed shear of 7.2×10^{-3} s^{-1}. In all three regions, the core varies in altitude with time, ascending and decreasing in intensity just after it has reached the lowest height.

Naturally, the aforementioned wind speed peak-times are related to the static stability of the lower troposphere. The diurnal behavior of the mean potential temperature field in the 950–800-hPa layer, depicted in Fig. 2.8, shows that the lowest air temperatures along the OLLJ corridor occur around 0700 LST (Fig. 2.8d) and the highest air temperatures around 1500 LST (Fig. 2.8f). Therefore, the time of occurrence of the OLLJ minima wind speeds (i.e., 1500 LST) coincides with the time of the maxima potential temperatures, when the boundary layer is almost unstratified. Nevertheless, the same agreement is not found between the time of occurrence of the minima potential temperatures and the time of maxima wind speeds. Although both times coincide in the mid-corridor and exit regions (i.e., 0700 LST, when low-level static stability is maximized), the maxima mean wind speeds over the entrance region occur around midnight—at least six hours before the minimum mean potential temperatures.

2.4 Discussion

The performed spatial and temporal characterization of the OLLJ differs from that of previous authors, who described its presence only over Colombia (Vernekar et al. 2003), or only over Venezuela (Douglas et al. 2005; Labar et al. 2005; Torrealba and Amador 2010; Rife et al. 2010). Ironically, Rueda (2015) mentioned the origin of the OLLJ in Venezuela, but its characterization was done almost entirely over the Colombian Llanos. Furthermore, despite Torrealba and Amador (2010) providing spatial dimensions to the phenomenon (1200 km in length and 400 km in width), they did not find more than one core, nor did any of the other authors. Also, none of them described the core height varying depending on geographical location.

The seasonal minimum wind speed of the LLJ was established by Douglas et al. (2005), Labar et al. (2005), and Torrealba and Amador (2010) as occurring in November, whereas the maximum wind speed occurred in February, one month later than the maximum monthly mean wind speed found in this study. However, the monthly wind-speed horizontal plots generated from reanalysis by Rueda (2015) using a more extended period (1983–2003), depict the maximum wind intensities and longest extension of the OLLJ in January, in accord with the results described in the present article. This one-month difference may be due to the influence of the ENSO warm phase since Douglas et al. (2005), Labar et al. (2005), and Torrealba and Amador (2010) used similar pilot balloon/radiosonde data sets (2001–2006)—most of them during El Niño years.

Besides the differences mentioned above in the main characteristics and austral-summer evolution, differences in the diurnal behavior are also meaningful because the OLLJ is a dynamical phenomenon that hourly evolves in geographical location, height, and intensity. Previous authors described the OLLJ almost as a spatially fixed structure, diurnally varying only in wind speed. However, the increased spatial and temporal resolutions make evident the diurnal core height variation over (e.g., Fig. 2.6c and 2.6f; Fig. 2.7c and 2.7i) and among locations (e.g., Fig. 2.6d–2.6f; Fig. 2.7a–2.7c), the geographical displacement of the core under the influence of sloping terrain (e.g., Fig. 2.6b and 2.6e), and the propagation in the along-stream direction of increasing wind speeds (Fig. 2.5).

One of the more interesting differences from previous studies is that the entrance region exhibits its maximum mean wind speed six hours earlier than the rest; consequently, it also starts weakening first, even before the other regions reach their corresponding maximum mean wind speed. That is, while the entrance region is in a weakening phase, in the rest of the OLLJ the strengthening phase is still ongoing.

Notwithstanding the early wind weakening at the entrance region, the results obtained in this study for the mid-corridor and exit regions, about the time of occurrence and magnitude of the maxima and minima mean wind speeds (0700 LST and 1500 LST, respectively), coincide reasonably with those found by Douglas et al. (2005) and Torrealba and Amador (2010) from observations at the inner part of the Venezuelan Llanos (i.e., over San Fernando de Apure and Guasdualito).

2.5 Summary and conclusions

The results on the OLLJ obtained from dynamical downscaling indicate that: (a) it is present over Colombia and Venezuela as a single stream tube with mean wind speeds greater than 8 m s^{-1}; (b) it has four distinctive LLJSs and different core heights at the entrance, mid-corridor, and exit regions (750 m AGL, 1200 m AGL, and 1500 m AGL); and (c) because of being ten times wider than deep (300 km × 3 km, approximately), it has an ellipsoidal vertical shape.

The OLLJ is present from November to March, displaying the least monthly wind speed (~9 m s^{-1}) in November and the greatest spatial reduction (~1500 km in length) in March, whereas its greatest monthly wind speed (~13 m s^{-1}) and longest and widest extension (2100 km × 400 km) occur in January. In this month, the OLLJ even becomes a cross-equatorial phenomenon.

The intraseasonal variability of the wind speed and potential temperature only presents significant periodicity in the diurnal and semidiurnal scales, with no other meaningful cycles evident during the Austral summer.

The OLLJ exhibits diurnal maxima mean wind speeds (~12–15 m s^{-1}) in the morning (0700 LST), when the potential temperatures in the 950–800-hPa layer are the lowest, and minima mean wind speeds (~9 m s^{-1}) in the afternoon (1500 LST), when the potential temperatures in the layer are the highest. However, this correspondence is not true for the entrance region where the maxima mean wind speeds (~15 m s^{-1}) occur early in the cycle (~0000 LST).

The maximum mean wind speed and the lowest mean height of the core are reached at the same time, but this height depends on geographical location. For the entrance and mid-corridor regions, the lowest core altitude is 500 m AGL and 700 m AGL, respectively, whereas for the exit region the lowest core altitude is 1250 m AGL. After reaching its lowest height, the core ascends and decreases in intensity.

Compared against the results from previous authors, dynamical downscaling is demonstrated to be an effective method to better resolve the horizontal and vertical characteristics of the OLLJ, not only improving the identification and location of LLJSs inside the stream tube, but also its diurnal and austral-summer evolution. Further research including additional years is required to determine the influence of longer time scale phenomena (e.g., ENSO, MJO) on the interannual and intraseasonal variability, which was outside the scope of this work.

Tables and Figures

Table 2.1: WRF-ARW model configuration.

Numerical and physical process	Schemes and model
Microphysics	Thompson graupel scheme (Thompson et al. 2008)
Longwave radiation	Rapid Radiative Transfer Model for GCMs (RRTMG) longwave scheme (Mlawer et al. 1997; Iacono et al. 2008)
Shortwave radiation	RRTMG shortwave scheme (Mlawer et al. 1997; Iacono et al. 2008)
Land surface	NOAH land-surface model (Chen and Dudhia 2001)
Planetary boundary layer	MYNN2 Mellor-Yamada Nakanishi and Niino Level 2.5 (Nakanishi and Niino 2006)
Cumulus parameterization	Kain–Fritsch (Kain 2004)

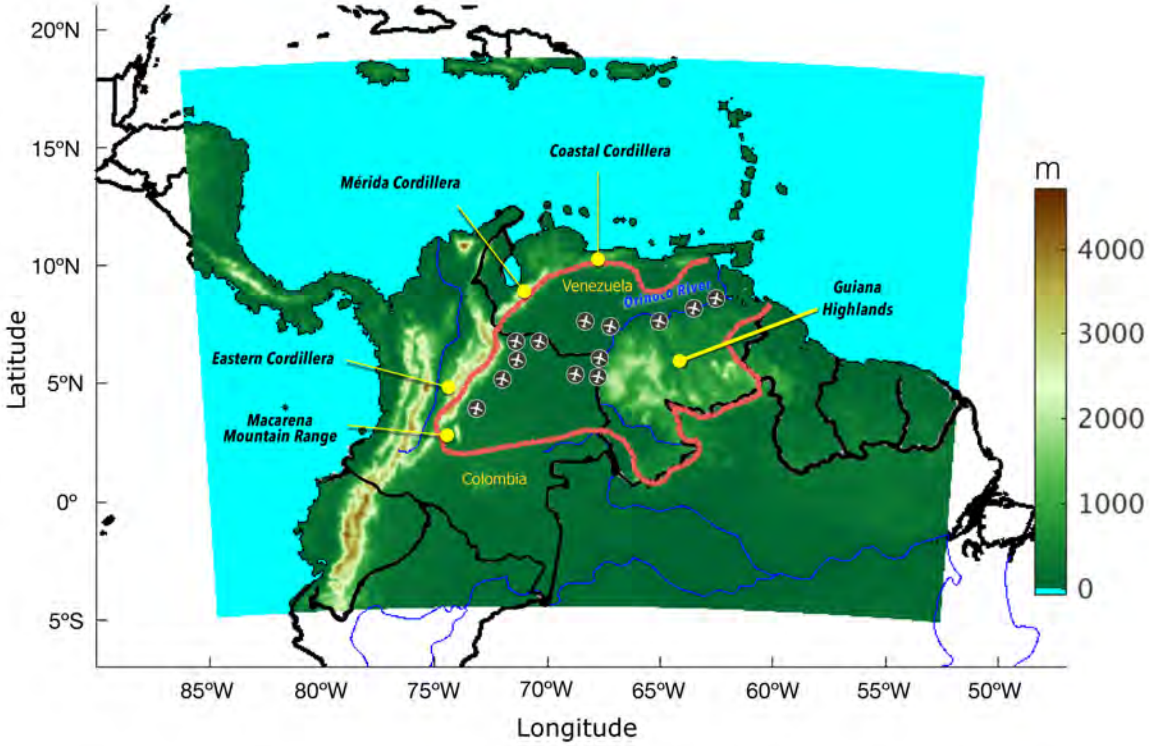

Figure 2.1: Topographic map of northern South America showing the Weather Research and Forecasting (WRF) model domain (colors), the Orinoco River basin limits (red), and locations of the main airports along the OLLJ corridor.

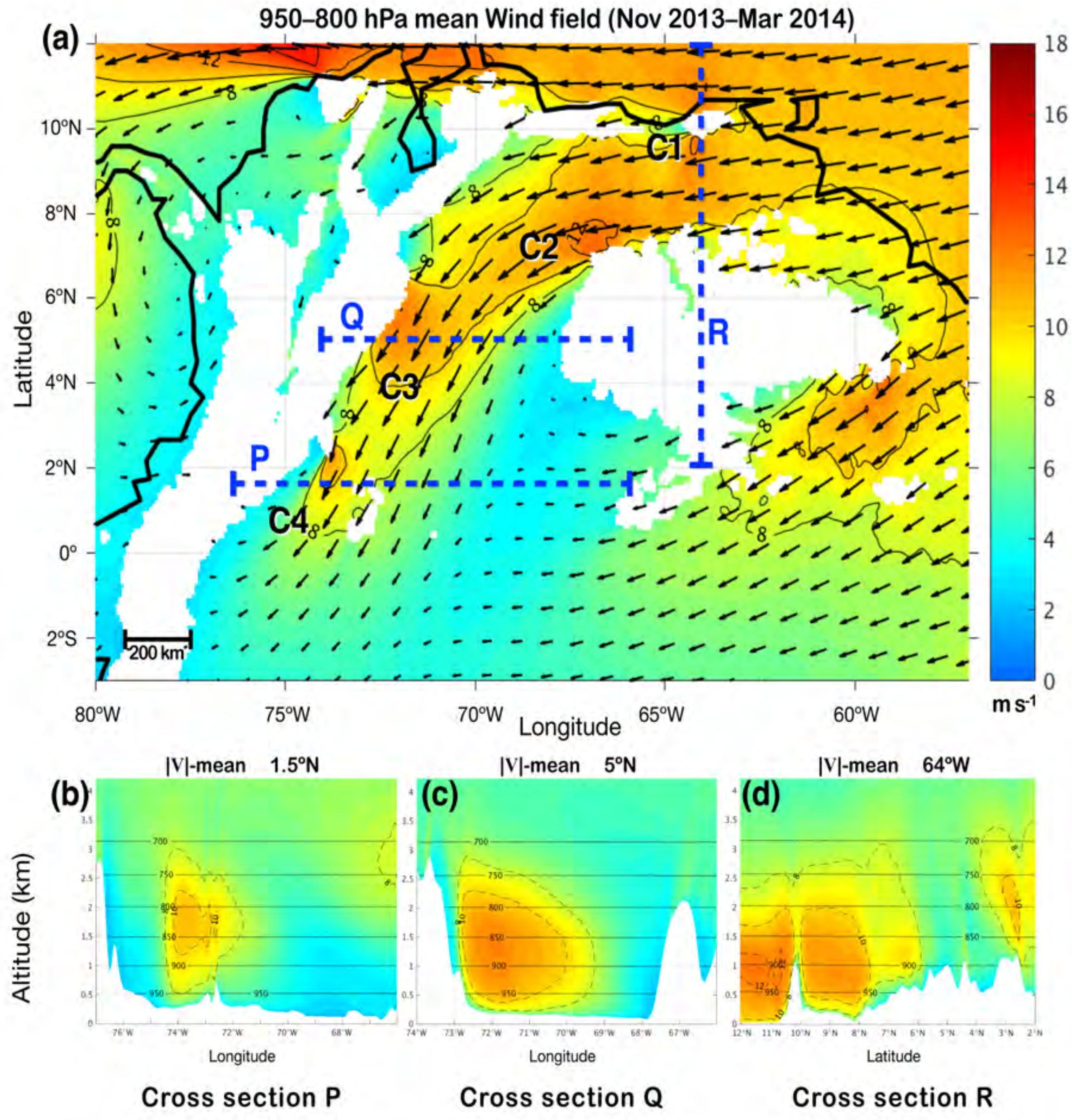

Figure 2.2: Horizontal and vertical characterizations of the OLLJ mean wind field (November 2013–March 2014). (a) Velocity vectors and average wind speed (shaded, m s^{-1}) in the 950–800-hPa layer, and vertical cross-sections of the mean wind speed at (b) 1.5ºN, (c) 5ºN, and (d) 64ºW. The main LLJS locations are indicated in bold black (C1–C4) and the limits for each vertical cross-section in (b)–(d) are shown by blue dashed lines (P, Q, R) in (a).

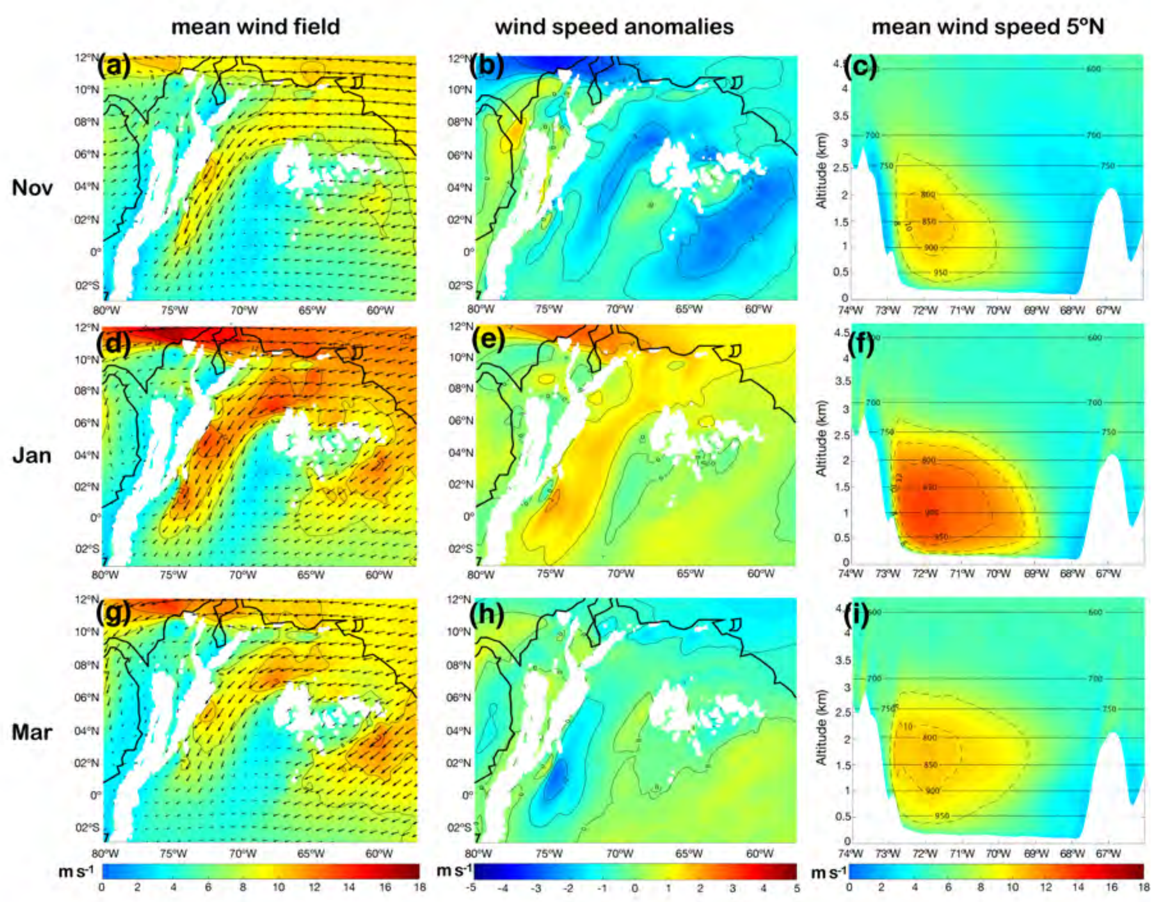

Figure 2.3: Horizontal and vertical characterizations of the OLLJ austral-summer evolution (November 2013–March 2014). The monthly 950–800-hPa-layer velocity vectors and wind-speed average (shaded, m s^{-1}) in (a), (d) and (g), the monthly 950–800-hPa-layer mean wind-speed anomalies in (b), (e) and (h), and the vertical cross sections of the monthly mean wind speed at 5ºN in (c), (f), and (i). Only the onset in November, the peak in January, and the cessation/weakening in March are shown.

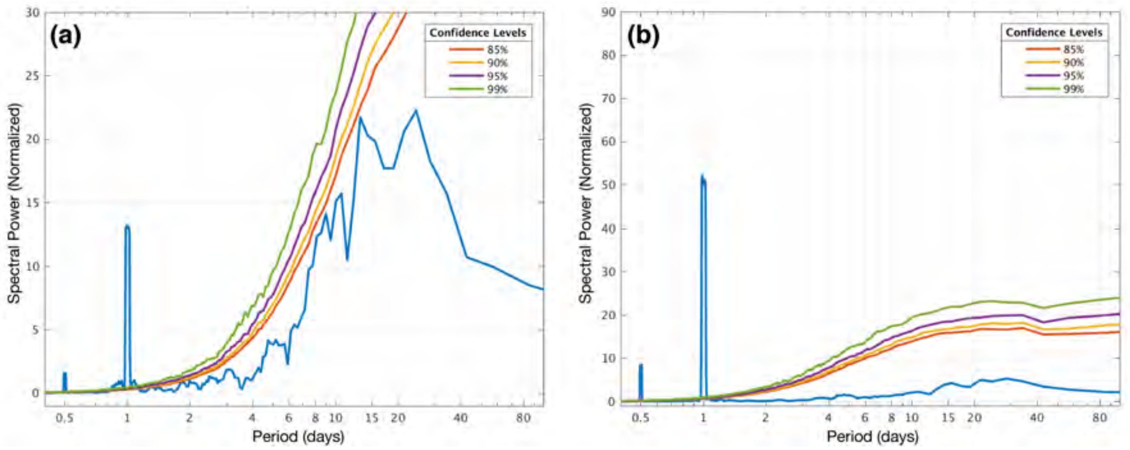

Figure 2.4: Normalized multitaper power spectral density estimate for (a) wind speed and (b) potential temperature time series at 5ºN–72ºW (C3 core) in the 900-850 hPa layer (blue line) during November 2013–March 2014. Colored lines indicate the level of confidence of the estimation, based on a Markov chain Monte Carlo, at 85% (red), 90% (yellow), 95% (purple), and 99% (green) regarding the amount of red noise in the signal.

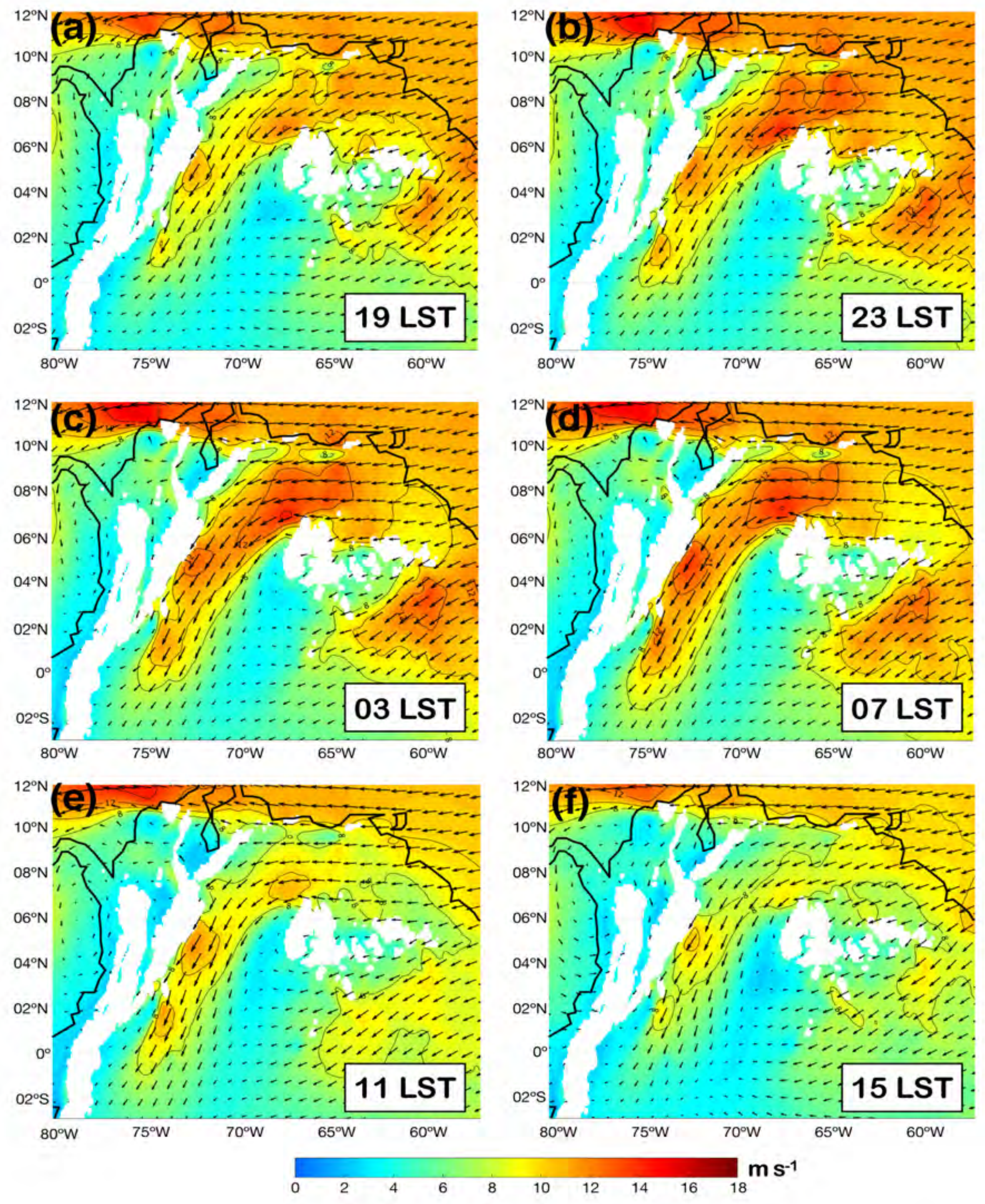

Figure 2.5: Diurnal variation of the 950–800-hPa-layer velocity vectors and wind-speed average (shaded, m s^{-1}) from November 2013–March 2014: (a) 1900 LST, (b) 2300 LST, (c) 0300 LST, (d) 0700 LST, (e) 1100 LST, (f) 1500 LST. Wind speeds greater than 8 m s^{-1} are contoured in 2 m s^{-1} increments.

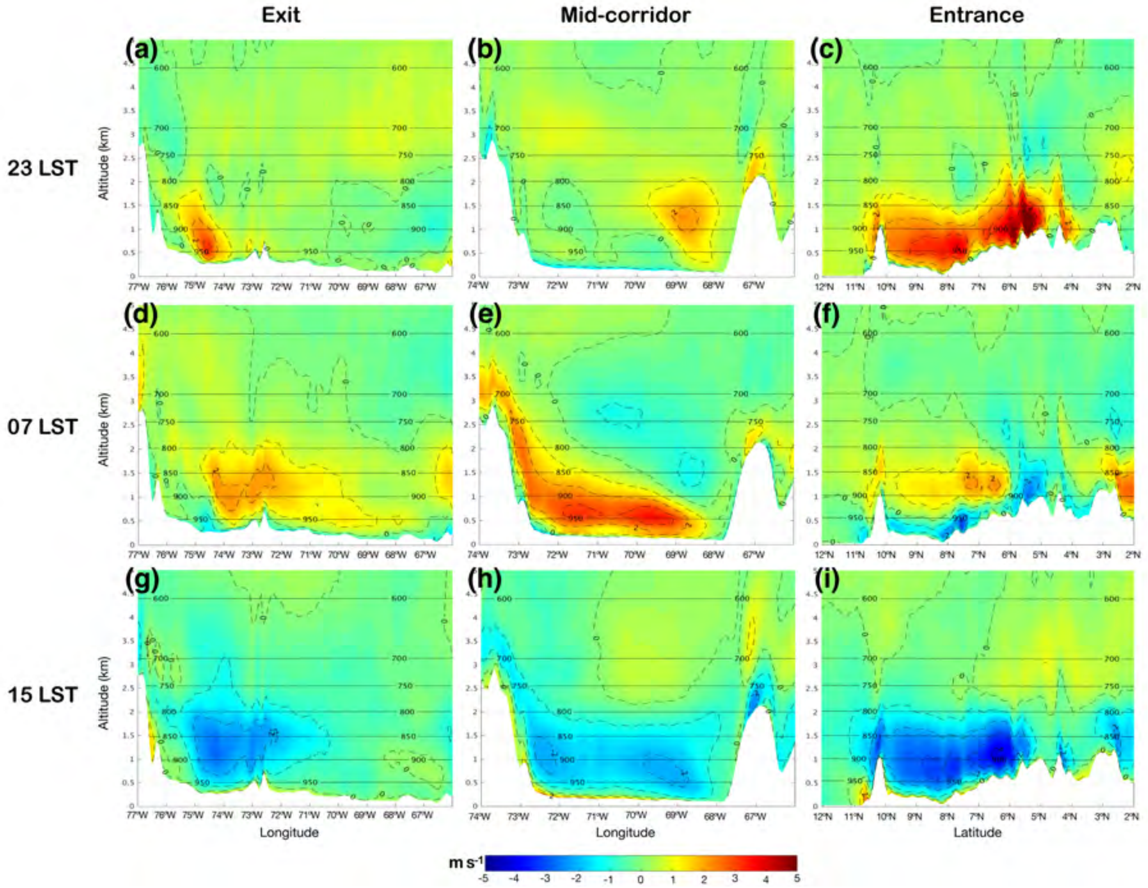

Figure 2.6: Diurnal variation of the wind-speed departure from its daily mean (shaded, m s^{-1}) at three locations along the OLLJ corridor: (c), (f), (i) at the entrance region (cross section R, Fig. 2.2); (b), (e), (h) at the mid-corridor region (cross section Q, Fig. 2.2); and (a), (d), (g) at the exit region (cross section P, Fig. 2.2). Wind-speed anomalies are contoured in 1 m s^{-1} increments with warm (cold) colors indicating positive (negative) anomalies.

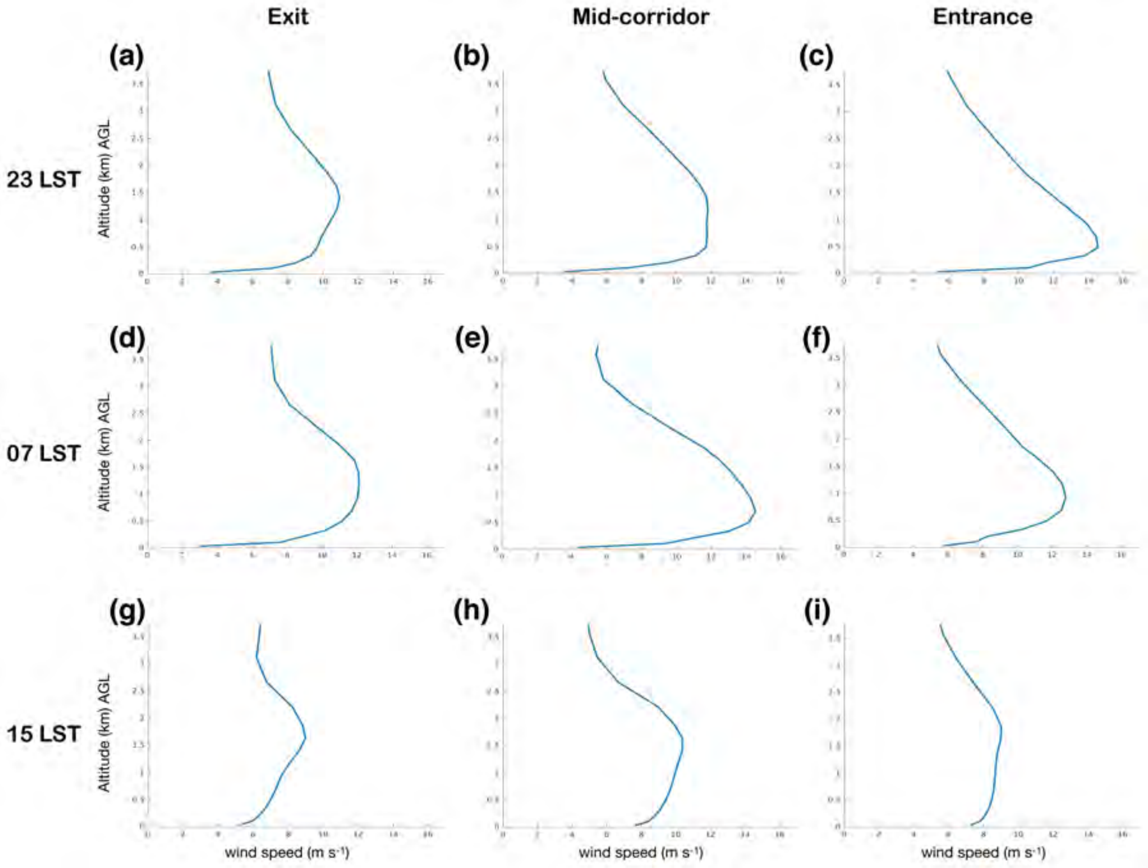

Figure 2.7: Diurnal variation of the wind-speed vertical profile during November 2013–March 2014 at three locations along the OLLJ corridor: (c), (f), (i) at the entrance region (cross section R, Fig. 2.2); (b), (e), (h) at the mid-corridor region (cross section Q, Fig. 2.2); and (a), (d), (g) at the exit region (cross section P, Fig. 2.2). Wind speeds in m s^{-1} and altitudes in km AGL.

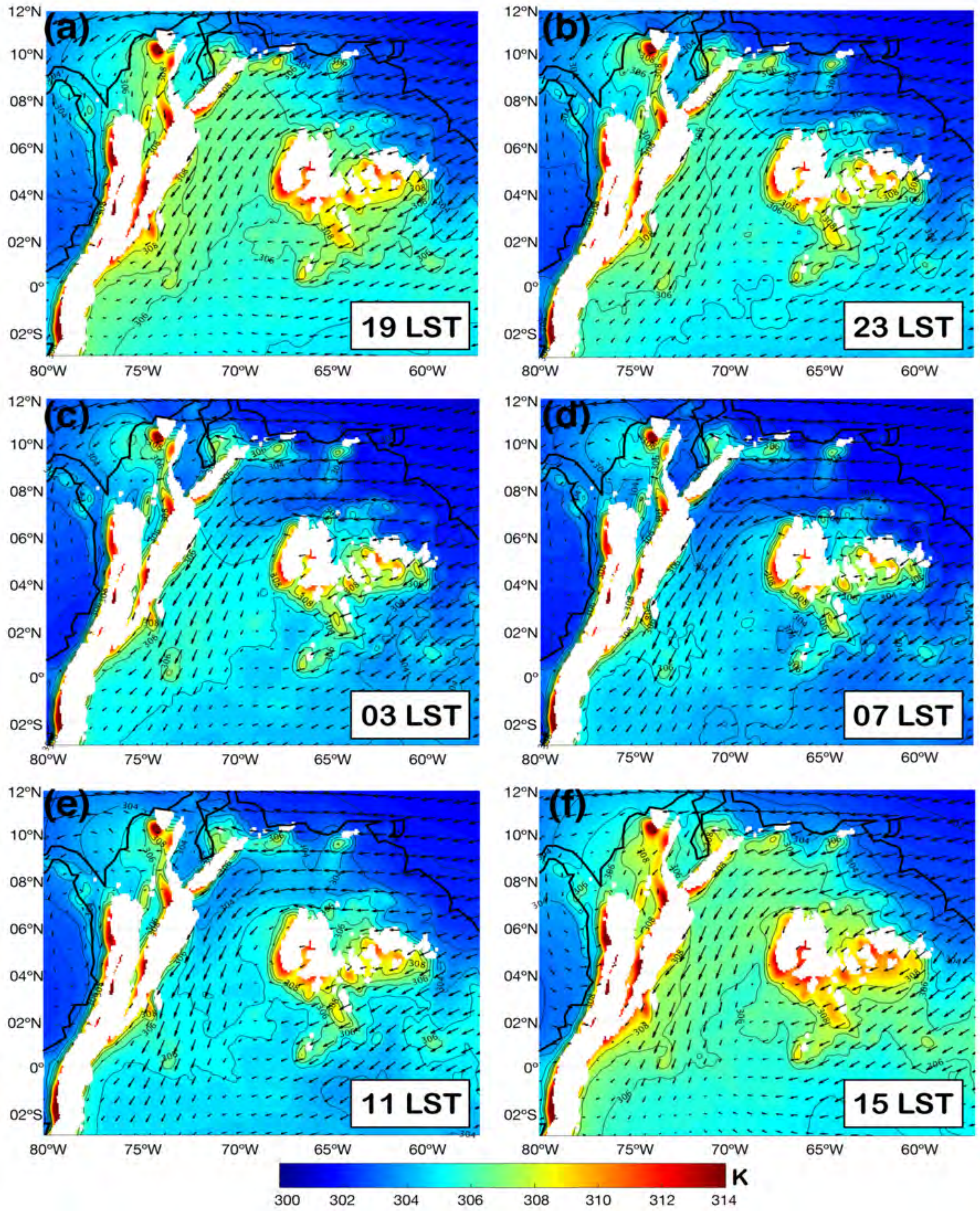

Figure 2.8: Diurnal variation of the 950–800-hPa-layer velocity vectors and potential temperature (K) average from November 2013–March 2014: (a) 1900 LST, (b) 2300 LST, (c) 0300 LST, (d) 0700 LST, (e) 1100 LST, (f) 1500 LST. Potential temperatures are contoured in 1 K increments.

Chapter 3

Mechanisms of Formation

3.1 Introduction

The occurrence of nocturnal low-level wind speed maxima—i.e., nocturnal low-level jets (LLJs)—is usually explained through the inertial oscillation and topographic thermal forcing mechanisms. The inertial oscillation mechanism, originally proposed by Blackadar (1957) and subsequently modified by Van de Wiel et al. (2010), attributes the acceleration of the wind to the imbalance of forces occurring at sunset once turbulent mixing ceases, which effectively leads to a vanishing of the drag force in the residual layer above the shallow stable nocturnal boundary layer (Stull 2015a). Without this frictional force, the horizontal wind accelerates, which in turn increases the Coriolis acceleration, ultimately causing the wind to oscillate about its geostrophic velocity. The velocity becomes most supergeostrophic when the ageostrophic wind component (its magnitude increases with an increasing frictional force acting on the upper-boundary-layer wind during the daytime period) rotates to an orientation aligned with the geostrophic velocity. Although the rotation rate of the ageostrophic velocity increases with latitude, the LLJ typically reaches its maximum wind speed 4–6 hours after sunset.

The topographic thermal forcing mechanism, introduced by Holton (1967), accounts for the effect that the diurnal oscillation of the horizontal temperature gradient over sloping terrain has on the direction of the thermal wind. At night, when the air adjacent to the slope cools more than the surrounding air at the same level, the thermal wind reverses its daytime direction, implying a poleward acceleration of the wind above the slope.

Both mechanisms may act together to produce an enhanced wind speed maximum, as is the case in the Great Plains LLJ (Bonner and Paegle 1970; Du and Rotunno 2014; Shapiro et al. 2016), or they can independently generate an LLJ (Stensrud 1996; Du and Rotunno 2014; Fedorovich et al. 2017); however, when only one of the mechanisms is present, the LLJ is usually untimely or weaker than observed (Du and Rotunno 2014; Shapiro et al. 2016). Recently, Parish (2017) stated that the inertial oscillation is the most important forcing in the Great Plains LLJ generation, giving only marginal relevance to the sloping-terrain diurnal heating variation. The development of a strong background pressure-gradient force (PGF), via long-term heating, is proposed to be of greater importance than the daily heating oscillations.

Although extensive research has been done on LLJs in the U.S. Great Plains (e.g., Blackadar 1957; Wexler 1961; Bonner 1963, 1968; Holton 1967; Bonner and Paegle 1970; Wu and Raman 1993; Whiteman et al. 1997; Song et al. 2005; Weaver and Nigam 2008; Squitieri 2014; Du et al. 2014; Krishnamurthy et al. 2015; Shapiro et al. 2016; Parish 2017), and in other parts of the world as well (e.g., Findlater 1969; Hart 1977; Virji 1981; Doyle and Warner 1993; Chen and Hsu 1997; Poveda and Mesa 1999, 2000; Liu et al. 2000; Zhao et al. 2003; Marengo et al. 2004; Rueda and Poveda 2006; Vera et al. 2006; Amador 2008; Muñoz et al. 2008; Rojas 2008; Wang et al. 2008; Whyte et al. 2008; Silva et al. 2009; Cook and Vizy 2010; Prabha et al. 2011; Giannakopoulou and Toumi 2012; Wei et al. 2013; Balmez and Ştefan 2014; Chen and Tomassini 2015; Du et al. 2014; Poveda et al. 2014; Soares et al. 2014; Du et al. 2015a,b; Hidalgo et al. 2015; Do Nascimento et al. 2016; He et al. 2016; Maldonado et al. 2016; Nicholson 2016; Maldonado et al. 2017; Juliano et al. 2017; Patricola and Chang 2017), just a few authors have investigated the low-level wind maximum occurring during the Austral summer in the savannas of the Orinoco River basin; hereafter referred as the Orinoco low-level jet (OLLJ).

The OLLJ became evident in the examination of the lower tropospheric winds from satellite images (Virji 1981) and reanalysis data (Montoya et al. 2001) over South America, but the existence of a larger-scale wind phenomenon (i.e., the South American low-level jet) concealed its detection. The identification and characterization of the OLLJ was subsequently achieved using mesoscale simulations (Vernekar et al. 2003; Rife et al. 2010), and a combination of pilot balloons, radiosondes, surface data, and more recent versions of reanalysis (e.g., Douglas et al. 2005; Labar et al. 2005; Torrealba and Amador 2010; Rueda 2015). However, no physical mechanisms of formation were investigated and, given the spatial and temporal limitations in observations and numerical model resolutions, only partial characterizations were obtained.

Vernekar et al. (2003), Labar et al. (2005), and Rueda (2015) have hypothesized that the OLLJ formation is related to the PGF between the North Atlantic subtropical high and the low pressure over Amazonia, when the Intertropical Convergence Zone (ITCZ)—also called the Near-Equatorial Trough (NET)—migrates southward during austral summer (Fig. 3.1a). As a result, the northeasterly trade winds strengthen while undergoing topographic channeling between the Coastal Cordillera and the Guiana Highlands. Diurnal heating and cooling of the basin, as well as differential heating between the mountains and the plains, the land and the ocean, produce changes in the vertical mixing of the air's horizontal momentum, modifying the OLLJ diurnal behavior. The studies performed by Rueda (2015) using ERA-Interim (1983–2013) showed that the OLLJ is only present from

November to March, whereas the rest of the year the northward migration of the ITCZ (Fig. 3.1b) weakens the LLJ and introduces southeasterly trade winds into the basin.

The purpose of this work is to investigate the physical mechanisms of formation of the OLLJ, by performing a dynamical downscaling of the large-scale atmospheric conditions provided by the Global Forecast System (GFS) analysis data, and a momentum balance evaluation similar to that used by Doyle and Warner (1993), Rife et al. (2010), Du et al. (2014, 2015a,b), and He et al. (2016). While the dynamical downscaling provides greater detail than in previous studies about the OLLJ structure and evolution, the momentum balance analysis decomposes the horizontal momentum equations to determine the physical forces causing the acceleration of the wind.

The findings suggest that the OLLJ is the result of several mesoscale mechanisms acting together to accelerate the wind, and because of its proximity to the equator, existing theories explaining the behavior of higher latitudes LLJs apply only partially to the OLLJ formation.

The next section describes the model configuration and momentum-balance analysis method. Section 3.3 analyzes the results and discusses the mechanisms of OLLJ formation. Finally, a summary and conclusions are presented.

3.2 Data and methods

3.2.1 Model configuration

To characterize the behavior of the OLLJ and the complex topography surrounding the Orinoco River basin, the nonhydrostatic version 3.4.1 of the Advanced Research-WRF model (WRF-ARW; Skamarock and Klemp 2008) is used to perform a dynamical downscaling of the large-scale atmospheric conditions. This modeling technique enables finer spatial and temporal resolutions than in previous studies. Figure 3.1 shows the limits of the model domain, which is centered at 7ºN and 68.5ºW, and the main topographic features along the OLLJ corridor.

The WRF-ARW physical parameterization schemes/models incorporate (i) the sub-grid turbulent kinetic Mellor-Yamada-Nakanishi-Niino-Level-2.5 (MYNN2; Nakanishi and Niino 2006) planetary boundary layer (PBL) scheme, (ii) the NOAH (National Centers for Environmental Prediction, Oregon State University, Air Force Weather Agency, and Hydrologic Research Lab) land-surface model (Chen and Dudhia 2001), (iii) The Kain–Fritsch (Kain 2004) cumulus parameterization scheme, (iv) the longwave and shortwave radiation Rapid-Radiative-Transfer-Model for GCMs (RRTMG) schemes (Iacono et al. 2008), and (v) the Thompson microphysics scheme (Thompson et al. 2008).

Through initial and boundary conditions provided by the 0.5º x 0.5º GFS Analysis (Unidata/University Corporation for Atmospheric Research et al. 2003), the WRF-ARW dynamical downscaling generates hourly regional analyses from November 2013–March 2014, at 9 km horizontal grid spacing and 51 vertical levels (from the surface up to 50 hPa). The domain has 407 × 284 grid points (3633 km × 2556 km). The boundary conditions are updated every 6 hours, starting at 1200 UTC 31 October 2013 until 1200 UTC 1 April 2014, and the model is reinitialized every four days to more closely resemble the known state of the atmosphere. The first 12-h integrations of each run are considered as the model spin-up time; therefore, they are not included in the analysis.

The period selected (November 2013–March 2014) provides the opportunity to analyze the OLLJ isolating the wind variability produced by El Niño-Southern Oscillation (ENSO), given that the Multivariate ENSO Index (MEI; Wolter and Timlin 1993) exhibits standard deviations not greater than 0.3×10^{-3} (i.e., ENSO neutral conditions). Additionally, it has been previously demonstrated that the OLLJ is an austral summer phenomenon (Montoya et al. 2001; Vernekar et al. 2003; Douglas et al. 2005; Labar et al. 2005; Rife et al. 2010; Torrealba and Amador 2010; Rueda 2015).

3.2.2 Momentum balance evaluation

Modifications to the WRF-ARW dynamical solver (Moisseeva and Steyn 2014) allows the extraction of the individual tendency terms from the horizontal momentum equations so that the contribution of each forcing to the total acceleration of the wind can be assessed. After the extraction, a streamwise (*s*) and a crosswise (*n*) coordinate system is constructed applying the dot product of the wind vector (**V**) to each tendency term. The final momentum equations characterizing the streamwise and crosswise components of the flow are:

$$\frac{\partial V_s}{\partial t} = -\frac{\partial \Phi}{\partial s} + (-\mathbf{V}\cdot\boldsymbol{\nabla}\mathbf{V})_s - fV_n + \mathrm{Res} \tag{1}$$

and

$$\frac{\partial V_n}{\partial t} = -\frac{\partial \Phi}{\partial n} + (-\mathbf{V}\cdot\boldsymbol{\nabla}\mathbf{V})_n + fV_s + \mathrm{Res} \tag{2}$$

Eqs. (1) and (2) enunciate that the local acceleration of the horizontal wind (LHS), along the streamwise and crosswise axes respectively, is balanced by the sum of the horizontal PGF, horizontal advection, Coriolis force, and Residual term. The residual includes accelerations due to the vertical momentum advection, map projection, model diffusion, and physical parameterizations, as well as errors in the calculation of the other terms in Eqs. (1) and (2). In the boundary layer, the residual is dominated by the effects of surface friction.

3.3 OLLJ conceptual model

The OLLJ is a single stream tube (2000 km long × 300 km wide × 3 km deep, approximately) over Colombia and Venezuela, with mean wind speeds greater than 8 m s^{-1}. It is an austral summer phenomenon that exhibits its seasonal maximum wind speed and largest spatial extent (2100 km × 450 km) in January (Fig. 3.2). The OLLJ's interaction with the surrounding topography produces four localized cores (C1–C4; Fig. 3.2) along its curved axis of propagation, whose mean heights above the terrain increase in the streamwise direction (~500 m, 700 m, 700 m, and 1250 m, respectively; Fig. 3.3).

The difference in time of occurrence of the diurnal maxima mean wind speeds at the center of each core location (Fig. 3.3), shows that there is an acceleration of the wind in the streamwise direction, with the maximum mean wind speed occurring at C1 around 2300 LST and C2 around 0400 LST; whereas at C3 and C4, the maxima mean wind speeds start approximately at 0700 LST and 0900 LST. The mean wind speeds are a minimum everywhere in the afternoon (~8 m s^{-1}, 1300–1600 LST). Table 3.1 summarizes the main characteristics of the OLLJ cores.

Based on the traditional mechanisms for LLJ formation (i.e., the Blackadar and Holton mechanisms), the acceleration of the wind should occur almost simultaneously at all locations once the upper-boundary-layer wind decouples from the surface layer; statically stabilized via radiative cooling, this layer impedes the upward propagation of frictionally retarded air. However, in the hourly 950–800-hPa-layer streamwise-acceleration field [$\partial V_s/\partial t$ in Eq. (1)] (Fig. 3.4) it can be seen that acceleration is not uniform across the domain; rather, there are distinct areas of acceleration coming from the Atlantic Ocean, the Caribbean Sea, and the Coastal Cordillera. Additionally, even though these mesoscale pockets of acceleration propagate in the streamwise direction, the C1–C4 wind-speed cores do not exhibit any propagation, just diurnal intensification (as shown in Fig. 3.3); they occur at precise locations (Fig. 3.2, Table 1).

Therefore, it is proposed herein that the OLLJ is the result of four mechanisms acting together to accelerate the wind over the valley of the Orinoco River basin, so producing a single wind structure that extends from the Orinoco delta to the Amazon forest. The four mechanisms, depicted in Fig. 3.5, involve (i) a sea-breeze penetration over the Orinoco River delta and Unare River depression, (ii) katabatic flow down the Coastal Cordillera, (iii) three expansion fans from point wakes in topography, and (iv) diurnal variation of turbulent diffusivity.

3.3.1 Sea breeze penetration

Sea breezes generated at the coastline along the Atlantic Ocean and the Caribbean Sea penetrate inland through the Orinoco River delta and Unare River depression. The relatively cool maritime air behind the sea-breeze fronts (SBF) is advected to the basin interior, and acting as gravity currents cause the wind to accelerate (i.e., the two mesoscale regions of positive acceleration at ~9ºN between 64ºW–66ºW in Fig. 3.4d). In the analysis, the maritime air is characterized by mixing ratios greater than 14 g kg^{-1}.

3.3.1.1 Orinoco delta region

The diurnal cycles of mean wind speed and potential temperature (Fig. 3.6) along the Orinoco delta region and Venezuelan Llanos (axis of propagation M in Fig. 3.5), show the sea breeze already established at 1100 LST (Fig. 3.6b), with a well-defined thermal internal boundary layer to the east of 64ºW; an indication that cool maritime air has advanced over the Orinoco delta region. As the day progresses, this denser air is advected further onshore, and once it reaches the western limit of the Guanipa Mesa (~64.5ºW) around 1500 LST (Fig. 3.6c), it flows downslope causing the wind to accelerate.

Because energy is conserved along an isentrope in dry-adiabatic motions, the acceleration of the wind, and consequently formation of the first OLLJ core (C1), is attained by transformation of potential energy into kinetic energy as the air on top of the Guanipa Mesa loses height downstream (see the bending isentropes at C1 locations in Fig. 3.6). A simple energy-transformation calculation for near midnight, using reduced gravity to account for the buoyancy effects opposing the gravitational force, yields just a –3 m s^{-1} difference with the wind speed given by the model, even though the nonhydrostatic effects of pressure were not considered.

The diurnal cycle of different surface variables at a selected point over the Guanipa Mesa (8.9ºN– 64.5ºW), shows evidence of the gravity-current nature of the sea breeze (Fig. 3.7). Starting at 1500 LST, a drop in potential temperature occurs, while there is an increase in surface pressure and mixing ratios; typical characteristics of the passage of a cool maritime density current (Simpson 1987, 1994).

3.3.1.2 Unare River depression

The Unare River depression is the ~100-km gap in the Coastal Cordillera that allows the river to discharge into the Caribbean Sea. This depression is connected to the Venezuelan Llanos and, because of the lack of prominent topographic features along its corridor (axis L in Fig. 3.5), enables the inland penetration of the sea breeze created therein. Based on an analysis of satellite imagery, Foghin-Pillin (2016) showed that this sea breeze penetrates up to 250 km in an SSW direction.

A well-established SBF around 10ºN (Fig. 3.8b), separating the cool maritime air from the statically-unstable mixed layer over the Llanos, starts advancing onshore around 1300 LST and reaches the limits of the Guiana Highlands (~ 7ºN) ten hours later (Fig. 3.8e); which implies a propagation speed of 8.3 m s^{-1}. Interestingly, gravity current theory predicts that under these atmospheric conditions the sea breeze should propagate at that very same speed. Once the cool air that has been accelerating behind the SBF arrives at the location of the C2 core (Fig. 3.5 and Fig. 3.8a, e, f), it merges with the latter so increasing the localized wind speed.

Impacts of the penetration of the sea breeze on the behavior of surface variables at a selected location (8ºN– 66.5ºW) along its axis of propagation L, can be assessed from Fig. 3.9, where starting at 1900 LST with the arrival of the SBF, there is a sudden increase in wind speed and a change in its direction from ENE to a less zonal NE (Fig. 3.9a). The southward advance of the sea breeze causes the rapid increase in the negative meridional component of the wind ($-v$) and the decrease in magnitude of the easterly component ($-u$). At the same time, the mixing ratio content and surface pressure exhibit a similar increasing rate of change, while the potential temperature continues dropping with a slight variation on its rate of change (Fig. 3.9b).

Therefore, the Unare sea breeze exhibits all the characteristics of a gravity current as proposed by Simpson (1987), Koch and Clark (1999), and Koch et al. (2005), namely:

- The observed (8.4 m s^{-1}; Foghin-Pillin 2016) and modeled speed of propagation (8.3 m s^{-1}) are consistent with that predicted from gravity current theory (C_{gc}= 8.3 m s^{-1}),
- there is a continuous cooling of the surface after the arrival of the SBF,
- a permanent rise in surface pressure, and
- the wind changes direction with an increase in speed.

Some of the instantaneous or short-lived shifts (i.e., rises or drops) expected in temperature and surface pressure upon the arrival of the SBF, cannot be determined due to the current specifications of the model. An even finer spatial and temporal resolution (< 1-km grid spacing and one-minute outputs) is needed to analyze this phenomenon with enhanced detail.

Stratified fluid dynamics also predicts that the intrusion of a gravity current into a less dense, two-layer, stably stratified fluid system, as the one existing ahead of the SBF at 1900 LST (Fig. 3.8d), may generate wave-like perturbations (e.g., bores, solitons), as occurs in Australia’s Gulf of Carpentaria (e.g., Clarke et al. 1981; Smith et al. 1982; Goler and Reeder 2004; Reeder et al. 2013) and other parts of the world (e.g., Koch and Clark 1999; Tsai et al. 2004; Coleman et al. 2010; Watson and Lane 2016). However, the Unare sea breeze does not spawn such perturbations because the depth of the gravity current is much larger (~ 5 times) than the thickness of the stable-stratified boundary layer being perturbed. In this case, the latter is mixed into the gravity current, causing it to behave as if the lower layer does not exist (Simpson 1987).

Furthermore, according to Koch and Clark (1999)—based on the modeling work of Haase and Smith (1989)—one of two parameters that determine if a bore can be generated from the intrusion of a gravity current is the ratio (μ) of the long gravity wave phase speed (C_o) to the gravity current speed (C_{gc}) [Eq. (3)], where N is the Brunt-Väisälä frequency, and h_o is the depth of stratified-boundary-layer inversion.

$$\mu = \frac{C_o}{C_{gc}} = \frac{2Nh_o/\pi}{C_{gc}} > 0.7 \tag{3}$$

For the Unare sea breeze, the calculated nondimensional value of $\mu = 0.28$ indicates that the flow is in the "supercritical regime" where the gravity current propagates faster than any gravity waves so that no bores can be generated. The ratio μ is calculated for 2000 LST when the stratified boundary layer ahead of the SBF is well established.

3.3.2 Katabatic flow

The contribution to the OLLJ streamwise acceleration coming from the Coastal Cordillera (i.e., mesoscale area of positive acceleration at ~9ºN– 68.5ºW in Fig. 3.4d) has its origin in two factors: the radiative cooling of the southern slope near sunset, which produces shallow density currents; and the advection of cool maritime air over the top of the ridge. The diurnal variations of potential temperature and mean wind speed along the axis of propagation K (Fig. 3.10), show that the combination of these two factors starting around 1500 LST (Fig. 3.10b), cools down the hillside enough to generate a fast, cold downslope flow similar to that of a Bora phenomenon (Stull 2015b; Fig. 3.10c–f). The maximum wind speed over the lee slope (13 m s^{-1}) is attained at 2300 LST (Fig. 3.10e). Because the flow is supercritical (Froude Number = 2.4), once it reaches the lowlands it creates a nocturnal hydraulic jump, as suggested by the curved isentropes over the southern flank of the mountain (Fig. 3.10d–f).

As cool air continues flowing downslope the Coastal Cordillera, it acts as a gravity current with a leading edge around 9.2ºN at 1900 LST (Fig. 3.10d) that propagates up-valley during the night, weakening near 6ºN– 72ºW at 0200 LST (not shown) once it encounters a point wake in the Eastern Cordillera. Hence, this density current exhibits a ground speed of ~14 m s^{-1}, which results from the combination of the depth and magnitude of the negatively buoyant air (C_{gc} ~5 m s^{-1}), and the background wind speed (~9 m s^{-1}). The streamwise-acceleration area that follows this gravity-current leading edge ends up merging at 0300 LST around 7ºN– 70ºW with the trailing acceleration pocket originated by the sea breezes (Fig. 3.4f).

Evidence for this katabatic flow having the characteristics of a gravity current proposed by Simpson (1987), Koch and Clark (1999), and Koch et al. (2005), is given in Fig. 3.11, which shows the diurnal cycle of the wind field, potential temperature, surface pressure, and mixing ratio at a selected surface location (7.5ºN– 69.7ºW) along the axis of propagation K (Fig. 3.5). With the arrival of the gravity current at around 2200 LST, there is an increase in wind speed and a small change in its direction (Fig. 3.11a); meanwhile, a change in the rate of nocturnal cooling with a corresponding change in the increasing surface pressure rate is produced (Fig. 3.11b). The sustained increase in mixing ratio indicates the maritime origin of the gravity current.

In a similar way to the Unare and Orinoco-delta sea breezes, as the katabatic flow propagates over the Llanos and the near-surface layer ahead of it stably stratifies (via nocturnal radiative cooling), the intrusion of this denser current could generate waves in the form of bores or solitary waves. However, the evaluation of the ratio μ [Eq. (3)] yields a value of 0.12, so indicating that flow is supercritical and no waves can be spawned.

3.3.3 Point wakes and expansion fans

Previous studies have shown that supercritical-channel-flow hydraulic theory can be used to explain particular accelerating flow regions associated with bending topography in coastal environments (Winant et al. 1988; Samelson 1992; Söderberg and Tjernström 2001; Patricola and Chang 2017; Juliano et al. 2017). Since the OLLJ is a channeled flow bounded by topography and capped by the inversion at the top of the planetary boundary layer (PBL), the same hydraulic theory arguments are used herein to explain the preferred location of some of the OLLJ cores.

In a channel flow—represented by a two-layer shallow water model in which the lower layer is the PBL and the upper layer is the free troposphere—the ratio of the flow velocity to the speed of long gravity waves on the interface (i.e., the Froude Number, Fr) will determine the behavior of the flow when the vertical boundaries expand or contract. When Fr is supercritical (i.e., $Fr > 1$), because the speed of the flow is faster than the speed of any gravity wave generated, the effect of a change in the geometry of the channel cannot be communicated upstream, and all the information travels downstream in the mean flow. Thus, if the lateral boundary of the channel (e.g., shoreline topography, mountains) turns away from the mainstream, a hydraulic expansion fan is induced downwind, whereas if it turns closer to the flow, it produces a hydraulic compression jump.

Points (terrain prominences) along bounding topography mark the locations where the flow separates from the terrain—producing low-speed point wakes—or if under supercritical conditions remains attached to it, where expansion fans are generated. The characteristics of an expansion fan downwind of a point wake are lateral spreading of the flow, decrease in thickness of the PBL, and accelerating flow as a result of the conservation of the Bernoulli function (Winant et al. 1988; Samelson 1992; Söderberg and Tjernström 2001; Young and Winstead 2005; Patricola and Chang 2017). On the other hand, a low-speed point wake can be recognized as an extended region of low wind trailing downwind from the point (Young and Winstead 2005).

An illustration of the effect of expansion fans on the height of the PBL and, subsequently, on the wind speed, is depicted in Fig. 3.12, where the regions of maximum wind speed (closer to the surrounding topography) in the diurnal 500 m-AGL mean wind field coincide with the locations of low diurnal mean heights of the PBL along the OLLJ corridor. In the Orinoco River basin, as the large-scale wind flows through the valley, the mainstream is deflected by bending terrain, producing point wakes at three specific locations: the Guiana Highlands (Cerro La Emilia), Eastern Cordillera (Cerro Umpara), and Macarena mountain range (refer to cyan areas in Fig. 3.5). The regions of enhanced wind speed associated with their corresponding expansion fans, produce the C2–C4 cores depicted in Fig. 3.4. A summary of the main features of the point wakes and their associated phenomena is indicated in Table 3.2.

According to supercritical-channel-flow hydraulic theory, Fr and the angular change in the flow direction due to the bending boundary ($d\theta$), predict the final flow wind speed and PBL height depending on:

$$\sin\beta = \frac{c}{U} = \frac{\sqrt{g'h}}{U} = \frac{1}{Fr} \tag{4}$$

$$\frac{dU_n}{d\theta} = \frac{-U_n}{\cos\beta} \tag{5}$$

$$\frac{dU_n}{dh} = -\frac{g'}{U_n} \tag{6}$$

$$\frac{U^2}{2} + g'h = B \tag{7}$$

Where β is the angle of the expansion fan with respect to upstream flow, c is the gravity wave phase speed, U is the flow speed, g' is the reduced gravity, h is the PBL height, U_n is the component of the velocity normal to the wave that stems from the point where the boundary bends, and B is the Bernoulli function. The final depth of the PBL obeys the steady-state momentum equation [Eq. (6)], while the total velocity (if the flow is frictionless) follows Eq. (7).

At the northwestern Guiana Highlands, the terrain is oriented approximately in an ENE–WSW direction (Fig. 3.12), although around 7.2ºN–66.3ºW (Cerro La Emilia) the terrain angles approximately 13º southward. Because the channel width increase is small, the flow remains attached to the terrain, and the first expansion fan is produced. Given the boundary layer conditions upstream of the point wake, Eqs. (4)–(7) predict a PBL height downwind of ~600 m and a final wind speed of ~13 m s^1 as the flow accelerates to negotiate the 13º expansion, which indeed occurs (Fig. 3.12). Further downstream, the mountainous topography ends sharply, causing separation of the flow from the terrain and the generation of a low-speed point wake. The combination of an expansion fan and a low-speed point wake is known as a compound point wake (Young and Winstead 2005).

The wind speed core (C2) associated with this expansion fan is located over the Santos Luzardo national park in Venezuela, where it may be responsible for the Llanos del Orinoco aeolian landforms of dune systems described by Tripaldi and Zárate (2016). Such landform modifications by the wind are so strong and permanent that they are clearly visible in satellite imagery.

The second expansion fan is generated by the Cerro Umpara (6.6ºN–71.8ºW) where an approximately northerly flow is deflected 17º westward. The base flow at this location is transcritical, a pattern described by Rogerson (1999) where the main stream is supercritical in the vicinity of orographic bends but it is subcritical upwind.

According to the conditions of the flow around Cerro Umpara, and the hydraulic theory summarized previously, downstream of the orographic bend the flow accelerates and reaches ~12 m s^{-1} while decreasing the height of the PBL to ~600 m (Fig. 3.12). Because the main stream flows parallel to the Eastern Cordillera, the wind speed core (C3) created by the expansion fan is found downwind, attached to the sloping terrain.

This low-level wind maximum remains attached to the mountain under the effect of Coriolis force and PGF, which generate a net inward acceleration that traps the wind against the terrain. The 950–800-hPa diurnal cycle of streamwise and crosswise forces in a 36 km × 36 km-box (around 5ºN–72.5ºW) near the hillside (Fig. 3.13), shows that during the day the crosswise PGF and Coriolis forces (Fig. 3.13b) act together to accelerate the wind towards the mountain, causing a positive crosswise acceleration from 0900 LST to 1600 LST. At night, as friction is turned off due to the statically stabilization of the lower troposphere, the total crosswise accelerations are closer to zero (~2100–0600 LST), and the streamwise acceleration component (Fig. 3.13a) becomes predominant. In this period, the advection is the driving term in the total streamwise acceleration because it has the fastest response to adjust to the changes occurring in the PGF (Outten et al. 2009).

As the wind continues flowing equatorward, it encounters the Macarena mountain range oriented north-south, so the low-level flow is diverted southward and runs attached to the terrain. The third expansion fan occurs when the bounding topography bends ~10º westward, thus causing an acceleration of the flow, and a decrease in the PBL height downstream (Fig. 3.12). The base flow at this location is also transcritical, and because of the accelerating flow, the wind speed reaches ~ 11 m s^{-1}, so giving origin to the last of four OLLJ cores (C4). Once the mountain ends, the flow separates from the terrain, and induces a low-speed point wake on the Macarena mountain range lee, while the expansion fan lies eastward of it.

Given the above, supercritical-channel-flow hydraulic theory reasonable explains the localized characteristics of the C2–C4 regions, also predicting their final wind speed and PBL height.

3.3.4 Turbulent diffusivity diurnal variation

The Blackadar mechanism relies on the diurnal variation of turbulent diffusivity to produce an inertial oscillation of the horizontal wind, which eventually will generate the LLJ. Such inertial oscillation starts at sunset when turbulence diffusion in the boundary layer is reduced by statically stabilization of the surface layer (via radiative cooling) so that frictionally retarded air is no longer transported upward, and the wind above becomes frictionless and accelerates. As the magnitude of the horizontal wind increases so does the

Coriolis force, which makes the wind turn clockwise (counterclockwise in the Southern Hemisphere) and describe an oscillation around the geostrophic wind. At sunrise, radiative heating activates the turbulent mixing again, so friction adds to the force balance and the horizontal wind speed reduces to subgeostrophic values.

From a different perspective, this oscillation can be seen as the rotation of the ageostrophic wind in a circle centered on the geostrophic wind so that at some time during the night—which varies depending on the value of the Coriolis parameter *f* for each latitude—the ageostrophic wind has the same direction as the geostrophic wind. With both geostrophic and ageostrophic winds pointing in the same direction, the horizontal wind becomes supergeostrophic thus producing the LLJ.

In the hourly 950–800-hPa streamwise momentum balance at C1–C4 OLLJ cores (Fig. 3.14a–d), obtained by averaging a 45 km × 45 km box at the maximum wind speed location along 64ºW, 66.9ºW, 5ºN, and 1.5ºN respectively, the residual term (i.e., frictional effects) is the primary driving term causing total deceleration of the streamwise horizontal wind during daytime. On the other hand, during nighttime, when its value approaches close to zero (i.e., no frictional effects), the other forces in balance cause the positive streamwise acceleration of the wind. The latter is particularly true for the C3–C4 regions (Fig. 3.14c–d), whereas for the C1–C2 regions (Fig. 3.14a–b) the negative advection term shortens the total streamwise nocturnal acceleration cycle. The streamwise deceleration, initiated by the advection term at the C1–C2 regions, contributes to the early appearance of the maxima wind speeds, in comparison to the C3–C4 cores (Table 3.1), and is an indication of drainage flow (down valley) opposing the large-scale motions.

A supplemental illustration of the generalized effect of turbulent diffusivity diurnal variation is depicted in Fig. 3.4, where frictional decoupling of the 950–800-hPa wind after sunset cause the simultaneous streamwise acceleration of the flow over large areas across the domain (Fig. 3.4d), whereas the activation of turbulent mixing during daytime induce the overall deceleration of the wind (Fig. 3.4a, b). In a like manner, the diurnal evolution of the potential temperature contours and mean wind speeds at different locations (Fig. 3.6, 3.8, and 3.10) show that once the OLLJ has developed during nighttime (Fig. 3.6d–f, 3.8d–f, and 3.10d–f), the growth of the daytime convective boundary layer erodes the LLJ from below diminishing its mean wind speed (Fig. 3.6a–c, 3.8a–c, and 3.10a–c).

Interestingly, despite the turbulent diffusivity diurnal variation triggering the inertial oscillation, so causing the clockwise rotation of the horizontal wind at each of the core locations (not shown), the Blackadar mechanism does not strictly apply to all of them. The 950–800-hPa streamwise and crosswise diurnal cycle of the mean horizontal, geostrophic, and ageostrophic wind (Fig. 3.15), for the same locations as in Fig. 3.14, show that the maximum streamwise wind speed is the result of the combined streamwise geostrophic and ageostrophic winds at the C1 and C3 regions only (Fig. 3.15a, c), whereas the maximum wind speed in the C2 and C4 regions (Fig. 3.15b, d) results from a balance between the geostrophic and ageostrophic winds. In general, the horizontal wind in the C2 and C4 regions reflects such balance during the entire diurnal cycle. Moreover, the minimum wind speed is subgeostrophic at the C1 and C2 regions only, whereas it is supergeostrophic in the C3 and C4 regions. Strictly speaking, the minima wind speeds should be subgeostrophic everywhere, according to Blackadar's theoretical predictions.

Hence, the diurnal variation of turbulent diffusivity and subsequent inertial oscillation contribute to the OLLJ formation, although it plays a secondary role, especially close to the equator where the Coriolis parameter is so small that ageostrophic effects (e.g., changes in PGF due to terrain heating) drive the wind. The streamwise ageostrophic wind is, in general, of higher magnitude than the streamwise geostrophic wind in the C3 and C4 regions (Fig. 3.15c, d).

3.4 Summary and conclusions

Dynamical downscaling of the large-scale atmospheric conditions over northern South America, shows the presence of a low-level wind maximum occurring during the austral summer in the 950–800-hPa layer. This low-level wind maximum, herein identified as the Orinoco low-level jet (OLLJ), is a single stream tube (2000 km long × 300 km wide × 3 km deep, approximately) over Colombia and Venezuela, with mean wind speeds greater than 8 m s^{-1}. The OLLJ exhibits its seasonal maximum wind speed and largest spatial extent (2100 km × 450 km) in January, and its interaction with the surrounding topography produces four localized cores (C1–C4) along its curved axis of propagation.

In the diurnal cycle, the altitude of the cores increases in the streamwise direction (~500 m, 700 m, 700 m, and 1250 m AGL, respectively) under the influence of the sloped terrain. The maxima diurnal mean wind speeds (13–17 m s^{-1}) at each core location occur at different times during the night (2300, 0400, 0700, 0900 LST, respectively), thus showing an acceleration of the wind in the streamwise direction that starts in the Orinoco Delta and ends over the Amazon forest. The wind speeds are a minimum everywhere in the afternoon (~8 m s^{-1}, 1300–1600 LST).

Since acceleration of the flow is not uniform across the domain, as it is somewhat expected from the inertial oscillation and the topographic thermal forcing mechanisms, it is determined that the OLLJ is the result of four phenomena acting together to accelerate the wind over the valley of the Orinoco River basin, namely: the (i) sea breeze penetration over the Orinoco River delta and Unare River depression, (ii) katabatic flow down the Coastal Cordillera, (iii) three expansion fans from point wakes in the topography, and (iv) diurnal variation of turbulent diffusivity.

The continuous nocturnal advection of relatively cool air through the Orinoco delta region, Unare River depression (i.e., sea breezes penetration), and downslope of the Coastal Cordillera (katabatic flow), constitute a single density current that merges over the Llanos and propagates up-valley, causing acceleration of the wind behind its leading edge. Before combining over the Llanos, the Orinoco Delta sea breeze generates the C1 core as the advected cool maritime air flows downslope at the western limits of the Guanipa Mesa. Although density currents are known to spawn bores or solitary waves as they propagate in stably stratified environments, the size and propagation speed of the overall gravity current inhibit such behavior.

As the merged density current and large-scale flow move along the Orinoco River basin, the interaction with geographic points in the surrounding topography create point wakes at three fixed locations: the Guiana Highlands, Eastern Cordillera, and Macarena mountain range. Supercritical-channel-flow theory explains the expansion fans generated by these point wakes and properly predicts their final wind speeds and PBL heights. Such expansion fans give origin to the C2–C4 core regions.

A momentum balance budget performed for each one of the core locations shows that the diurnal variation of turbulent diffusivity decelerates (day) and accelerates (night) the horizontal winds across the domain, triggering the inertial oscillation mechanism and causing the clockwise rotation of the wind. However, opposite to what happens in higher latitudes, the role of the diurnal variation of turbulent diffusivity in the OLLJ acceleration is secondary, given that the maxima wind speeds as the result of combined geostrophic and ageostrophic winds occur in only two of the four cores. The cores closer to the equator (C3–C4) are driven by ageostrophic effects on the wind due to the large imbalance in the geostrophic wind as the Coriolis parameter f becomes small.

Although dynamical downscaling and the momentum equation decomposition improve the current OLLJ characterization and understanding about the dynamics behind its formation, additional contributions are yet to be resolved. For instance, what is the role of latent heat release over the Amazon forest on the strength of the LLJ? Would some form of the OLLJ still occur in the partial or complete absence of terrain? What is the overall contribution of the radiative heating to its formation? Does the OLLJ vary according to warm or cold ENSO phases? The answers to these uncertainties will allow the development of practical applications of the OLLJ for wind energy generation, aviation safety, fire weather prediction, oil-extraction pollutants transport, and public health, among others.

Tables and Figures

Table 3.1: Mean characteristics of the OLLJ cores.

	Core 1 (C1)	Core 2 (C2)	Core 3 (C3)	Core 4 (C4)
Geographical position	Guanipa Mesa, Venezuela	Santos Luzardo National Park, Venezuela	Fortul, Colombia	La Macarena, Colombia
Center location	9.5ºN– 64.2ºW	7.5ºN– 67ºW	5ºN– 72ºW	2ºN– 73.5ºW
Mean altitude (AGL)	~ 500 m	~ 700 m	~ 700 m	~ 1250 m
Maximum diurnal wind speed	~ 15 m s^{-1}	~ 17 m s^{-1}	~ 15 m s^{-1}	~ 13 m s^{-1}
Time of maximum wind speed	2300 LST	0400 LST	0700 LST	0900 LST

Table 3.2: Main characteristics of the point wakes.

	Guiana Highlands	Eastern Cordillera	Macarena Mountain Range
Geographic feature	Cerro La Emilia	Cerro Umpara	Serranía de La Macarena
Location	7.2ºN–66.3ºW	6.6ºN–71.8ºW	2.5ºN– 73.8ºW
Angular flow deflection	~ –13º	~ –17º	~ –10º
Hydraulic effect	Expansion fan	Expansion fan	Expansion fan
Associated OLLJ core	C2	C3	C4
Hydraulic theory predicted final wind speed*	13 ± 1 m s^{-1}	12 ± 1 m s^{-1}	11 ± 1 m s^{-1}
Model final wind speed	~13 m s^{-1}	~12 m s^{-1}	11-12 m s^{-1}
Hydraulic theory predicted final PBL height*	560 ± 110 m	460 ±150 m	600 ± 85 m
Model final PBL height	~600 m	~600 m	~650 m

**Uncertainties estimation procedure is presented in Appendix B.*

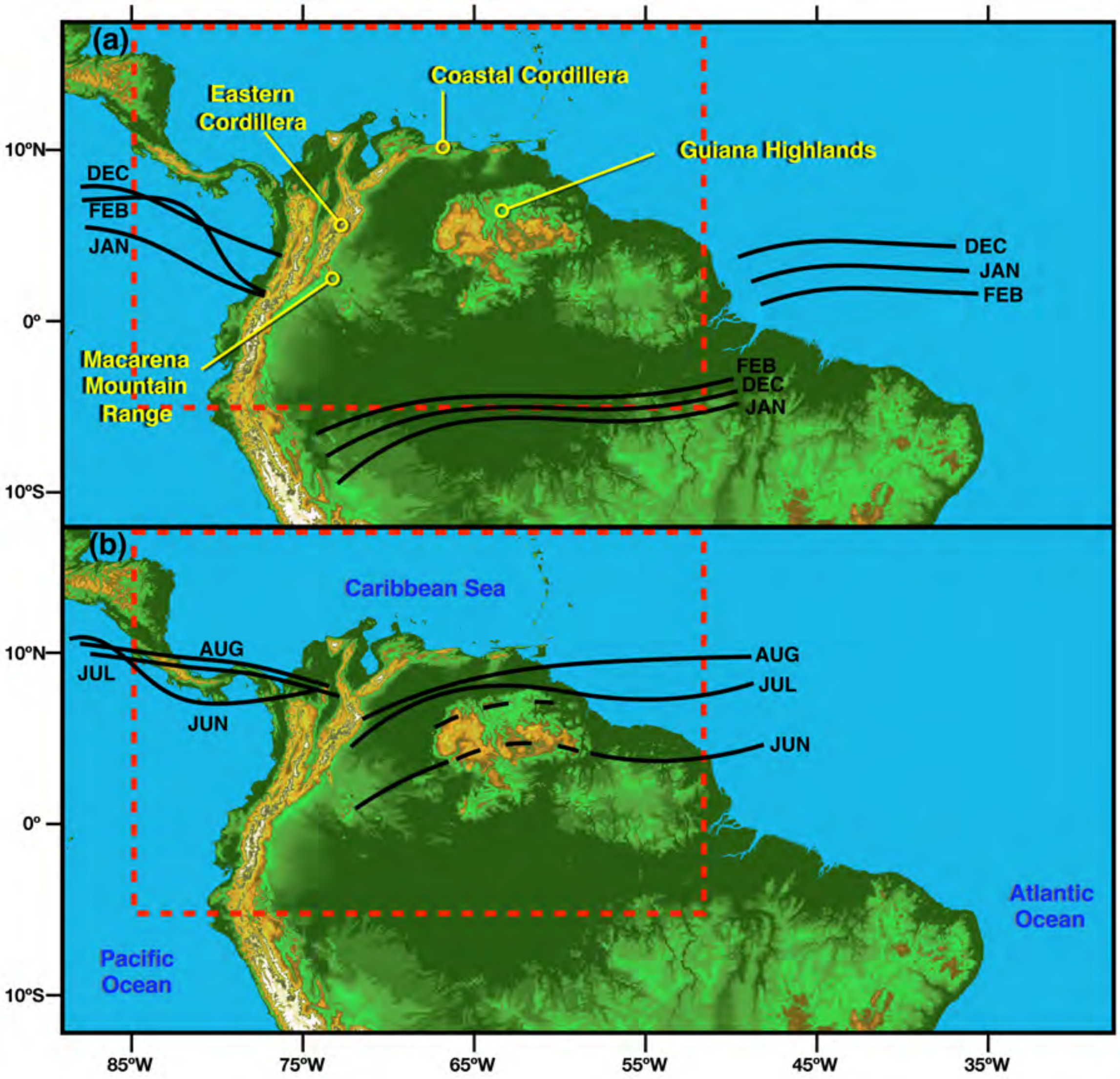

Figure 3.1: Map of northern South America displaying the mean Near-Equatorial Trough (NET) positions (black lines) during the (a) austral summer and (b) austral winter. Black dashed lines show two possible mean June positions. The mountainous terrain in the northern part of the continent breaks up the NET and makes the mean position variable [Adapted from Fig. 2-5 in Gilford et al. (1992)]. The limits of the WRF-ARW domain are shown in red.

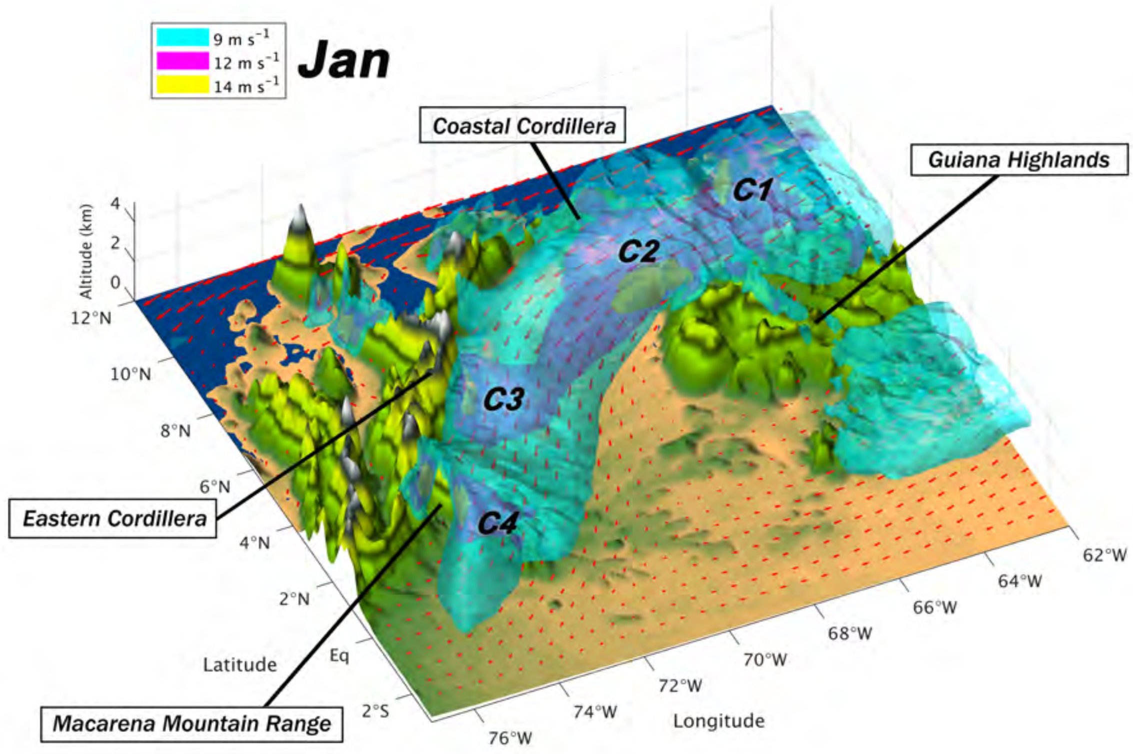

Figure 3.2: OLLJ-3D mean structure during January 2014, showing wind speed stream tubes of 9 m s^{-1} (cyan), 12 m s^{-1} (magenta) and 14 m s^{-1}. Interactions with surrounding topography produce localized cores (C1–C4). Lowland wind vectors at 500 m AGL are displayed in red.

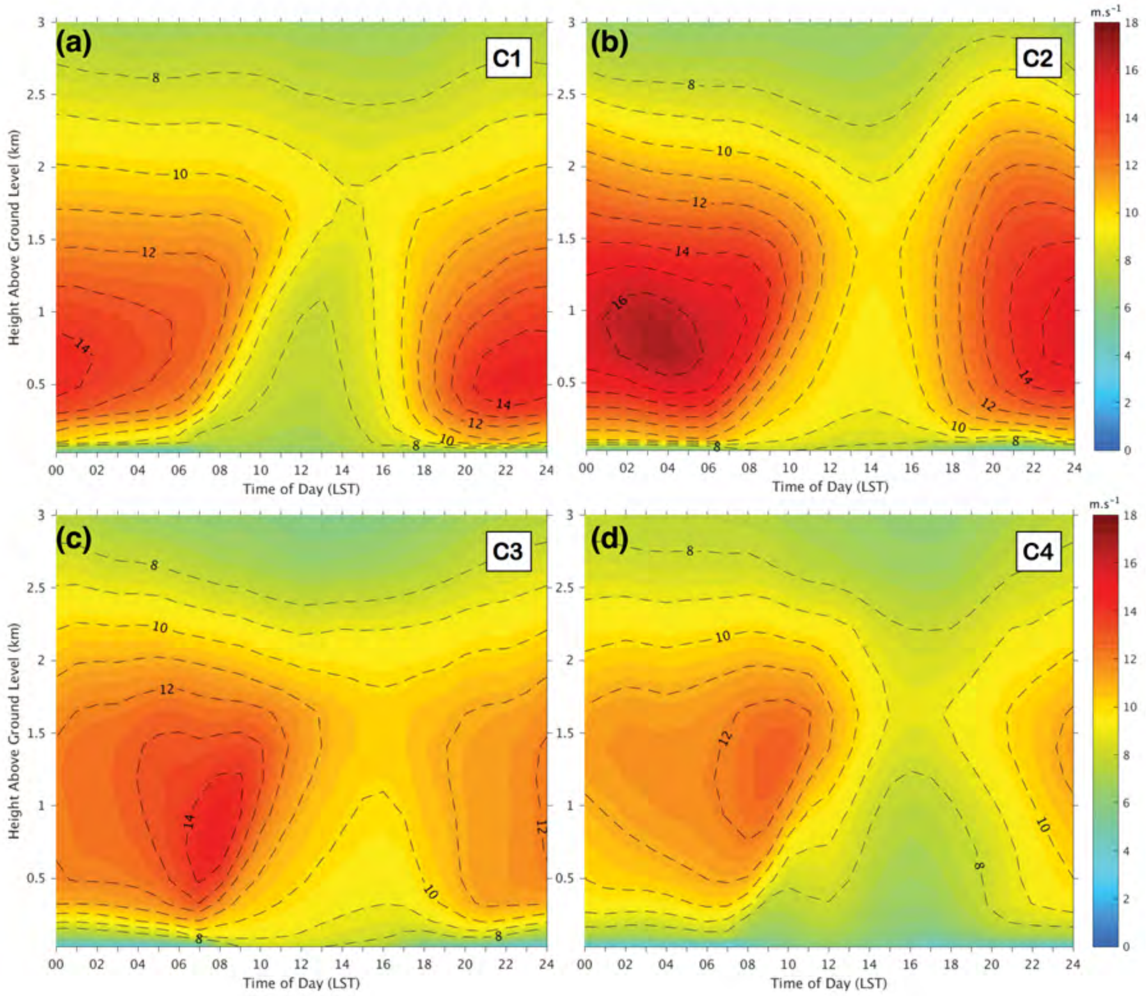

Figure 3.3: Time-height plot of hourly mean wind speeds from November 2013–March 2014 at each core location: (a) C1, (b) C2, (c) C3, and (d) C4. The differences in the time of occurrence of the maximum wind speed indicate an acceleration of the OLLJ in the streamwise direction.

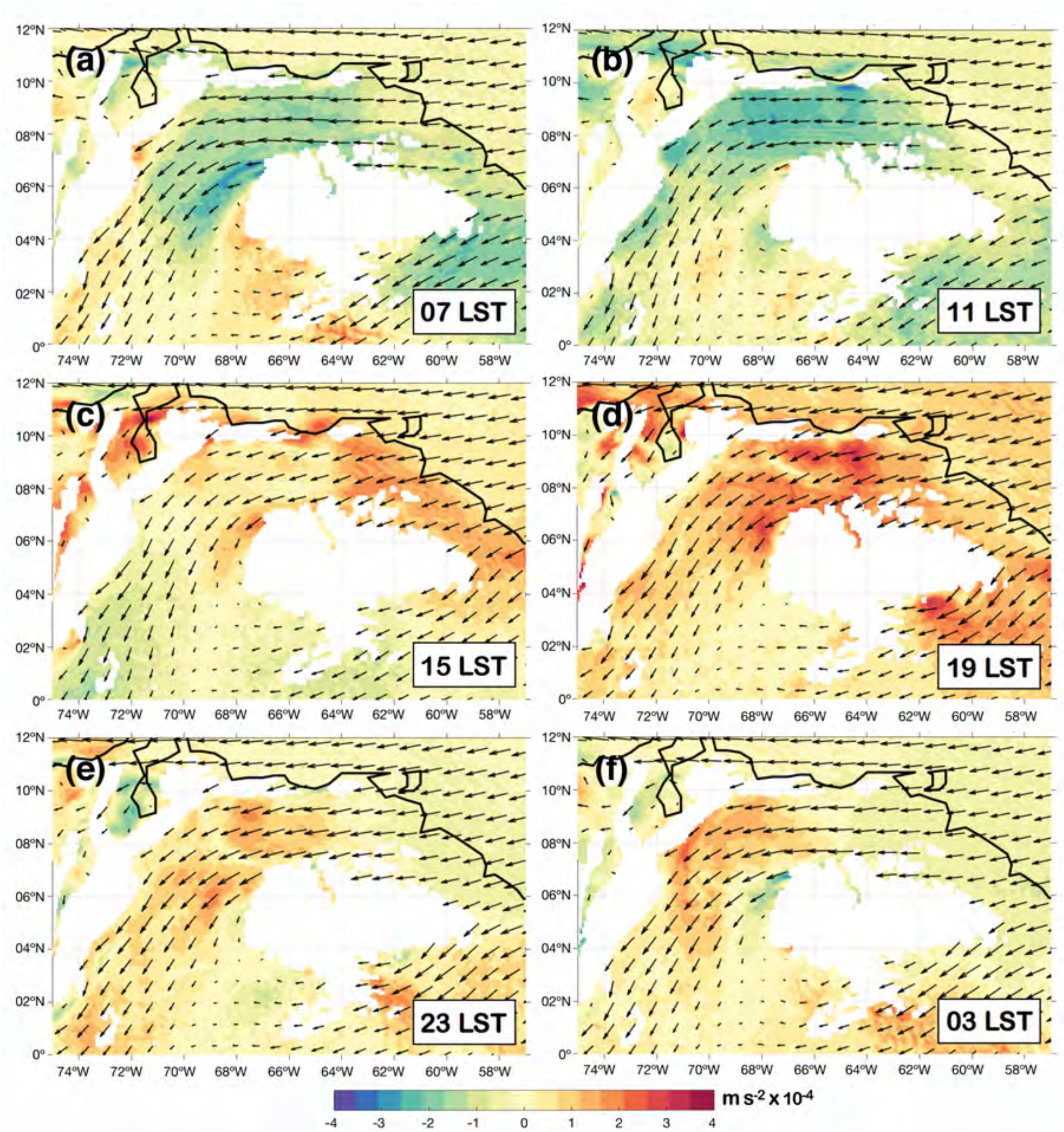

Figure 3.4: Diurnal variation of the 950–800-hPa-mean streamwise acceleration (shaded, m $s^{-2} \times 10^{-4}$) and wind vectors from November 2013–March 2014: (a) 0700 LST, (b) 1100 LST, (c) 1500 LST, (d) 1900 LST, (e) 2300 LST, (f) 0300 LST. Warm (cold) colors indicate acceleration (deceleration) of the wind.

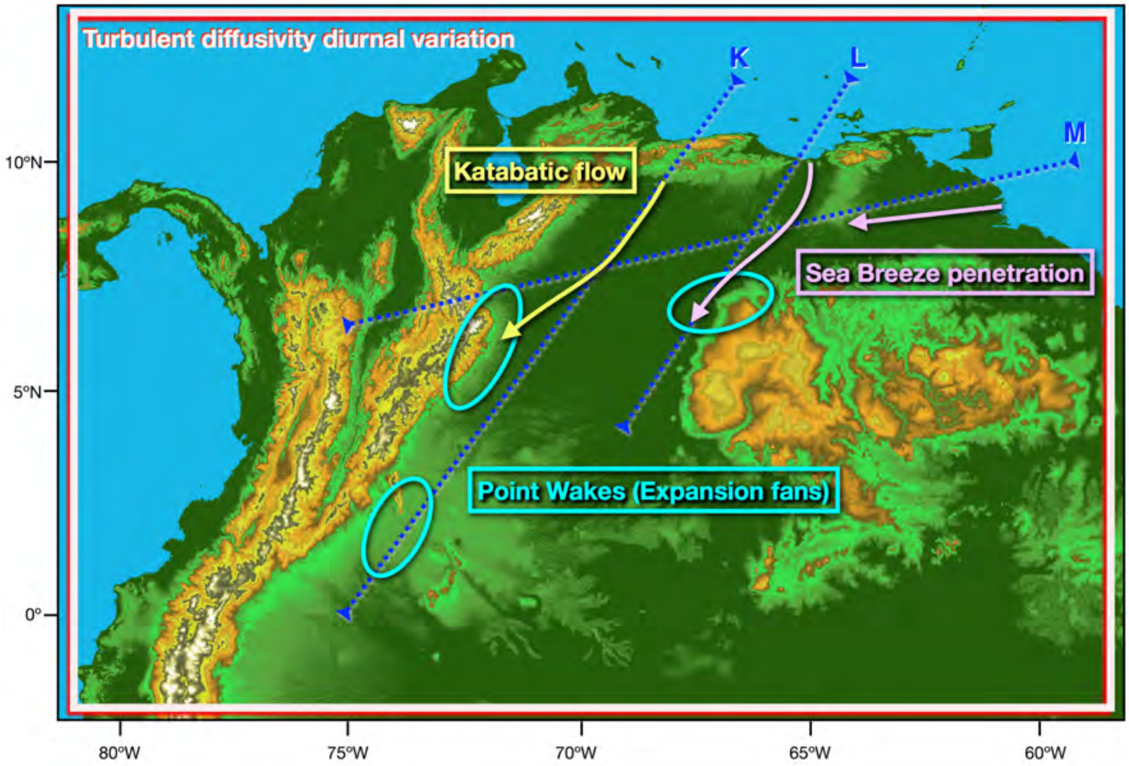

Figure 3.5: Locations of the four mechanisms causing the OLLJ. The limits of the cross sections along the axis of propagation of the Orinoco Delta (M) and Unare River (L) sea breezes, and Coastal Cordillera katabatic flow (K) are shown by dark blue dashed lines.

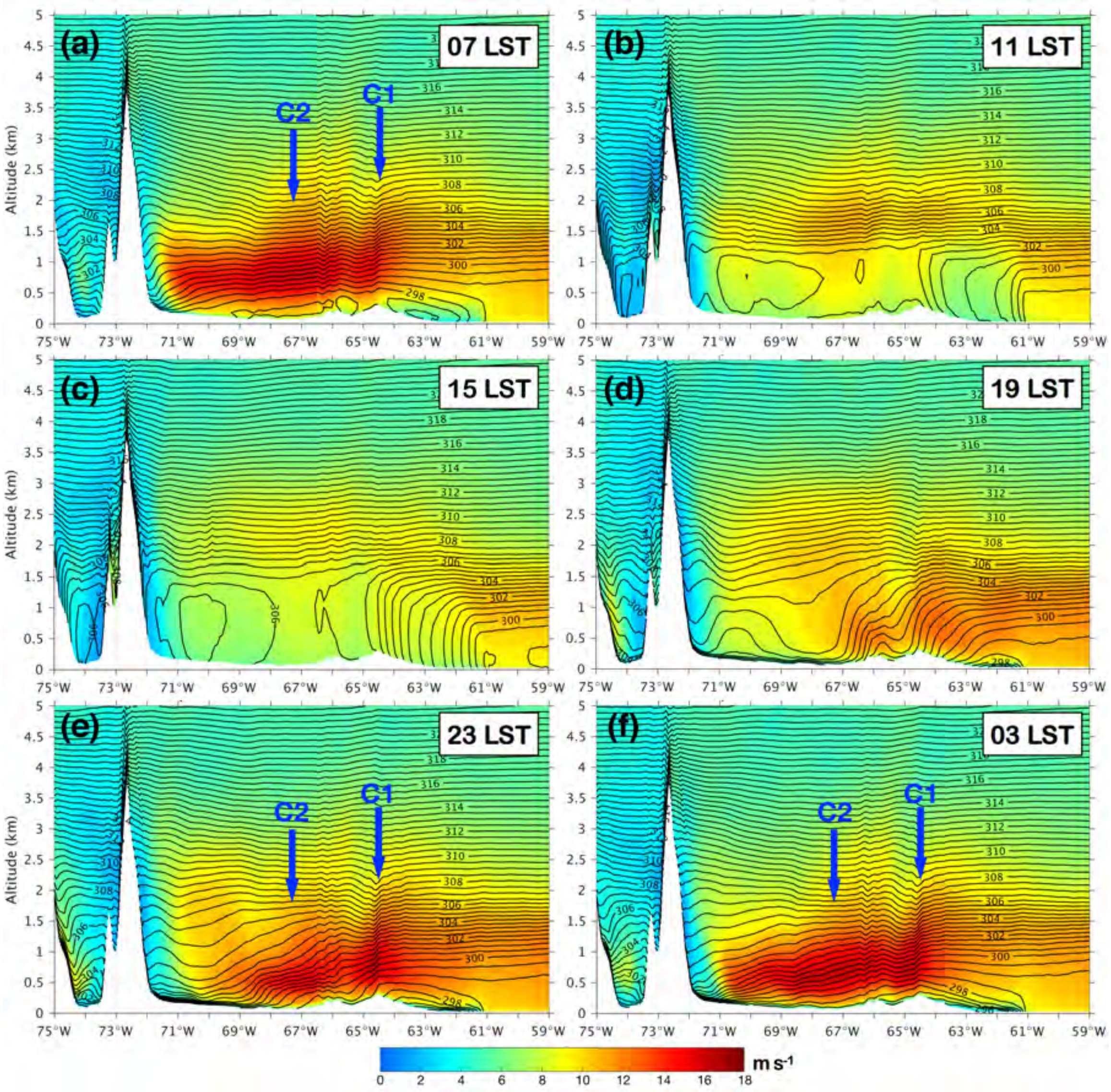

Figure 3.6: Diurnal variation of mean wind speed (shaded, m s^{-1}) and potential temperature (contoured, K), from November 2013–March 2014, in a vertical cross-section along the axis of propagation M (Fig. 3.5) at: (a) 0700 LST, (b) 1100 LST, (c) 1500 LST, (d) 1900 LST, (e) 2300 LST, (f) 0300 LST. The relative positions of the C1, C2 cores are also shown. Potential temperatures are contoured in 0.5 K increments.

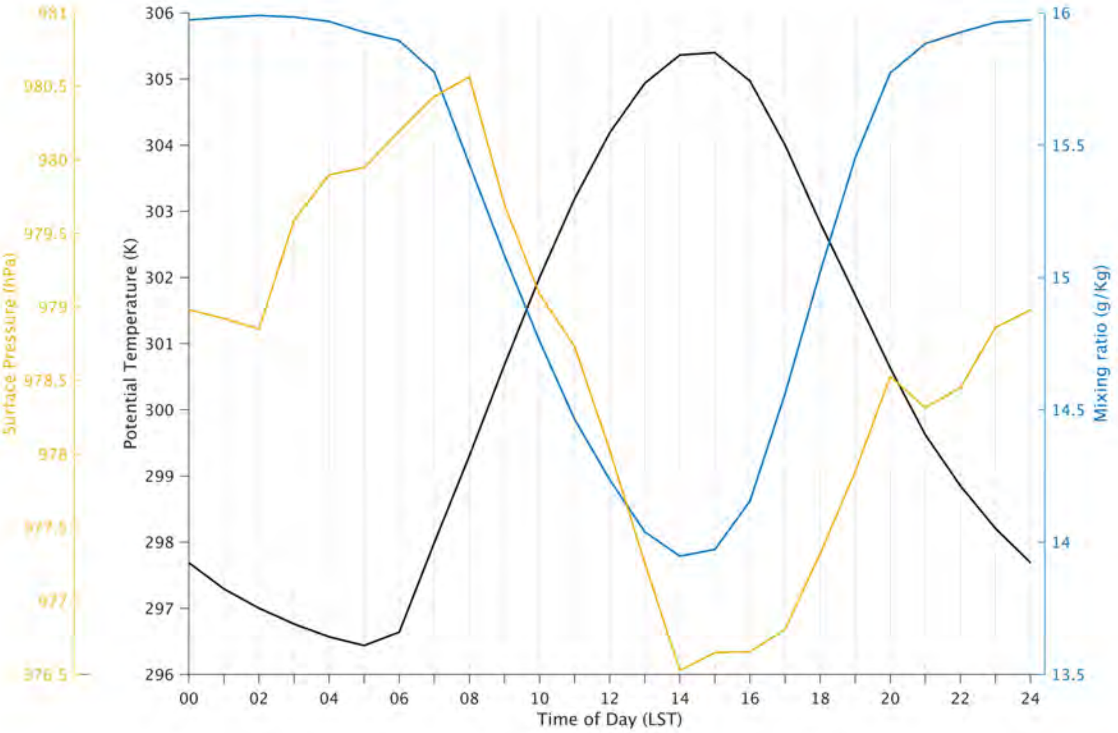

Figure 3.7: Diurnal cycle of surface pressure (yellow, hPa), potential temperature (black, K), and mixing ratio content (blue, g kg^{-1}), from November 2013–March 2014, at a surface location (8.9ºN– 64.5ºW) over the Guanipa Mesa (Venezuela).

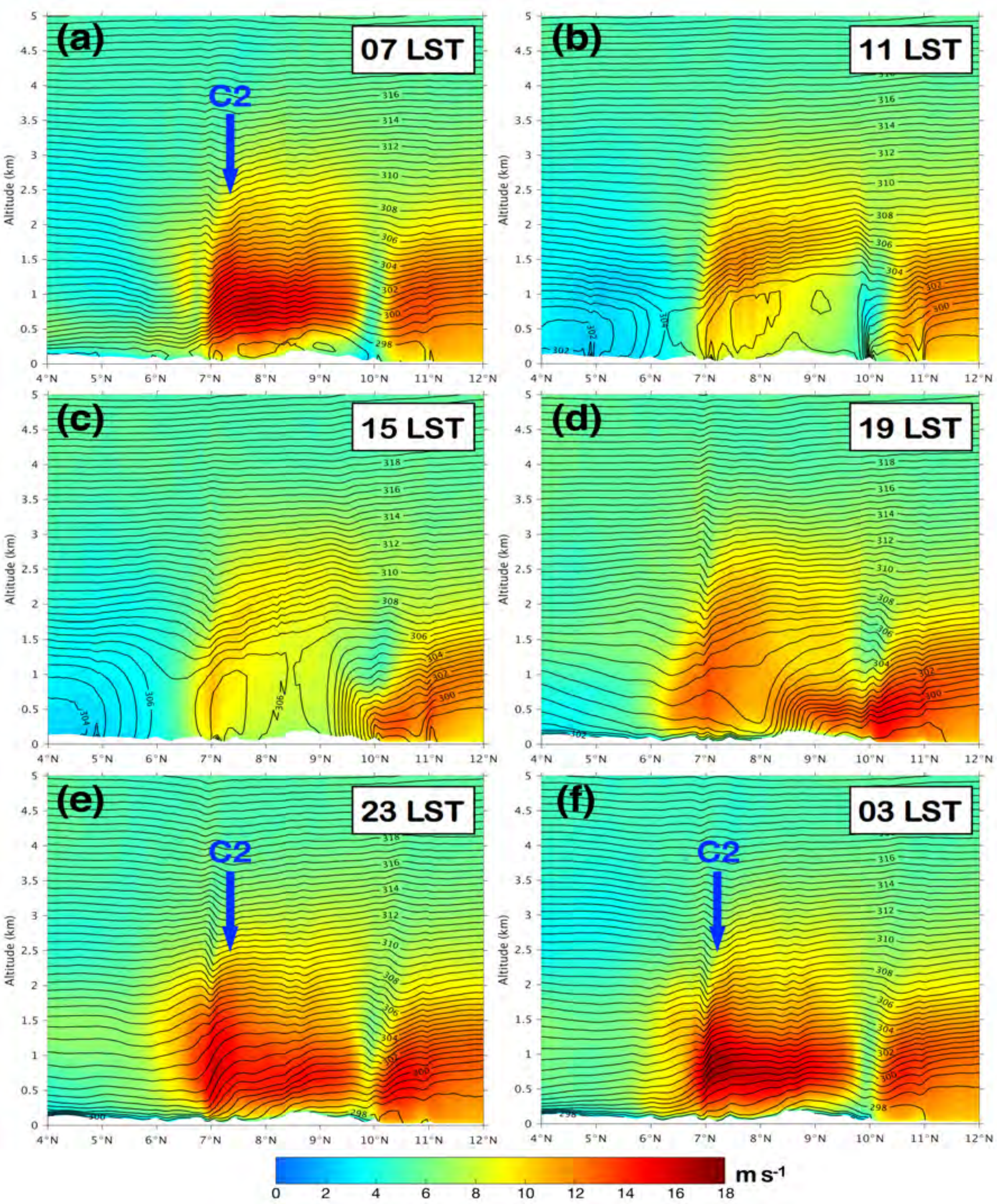

Figure 3.8: Diurnal variation of mean wind speed (shaded, m s^{-1}) and potential temperature (contoured, K), from November 2013–March 2014, in a vertical cross-section along the axis of propagation L (Fig. 3.5) at: (a) 0700 LST, (b) 1100 LST, (c) 1500 LST, (d) 1900 LST, (e) 2300 LST, (f) 0300 LST. The relative position of the C2 core is also shown. Potential temperatures are contoured in 0.5 K increments.

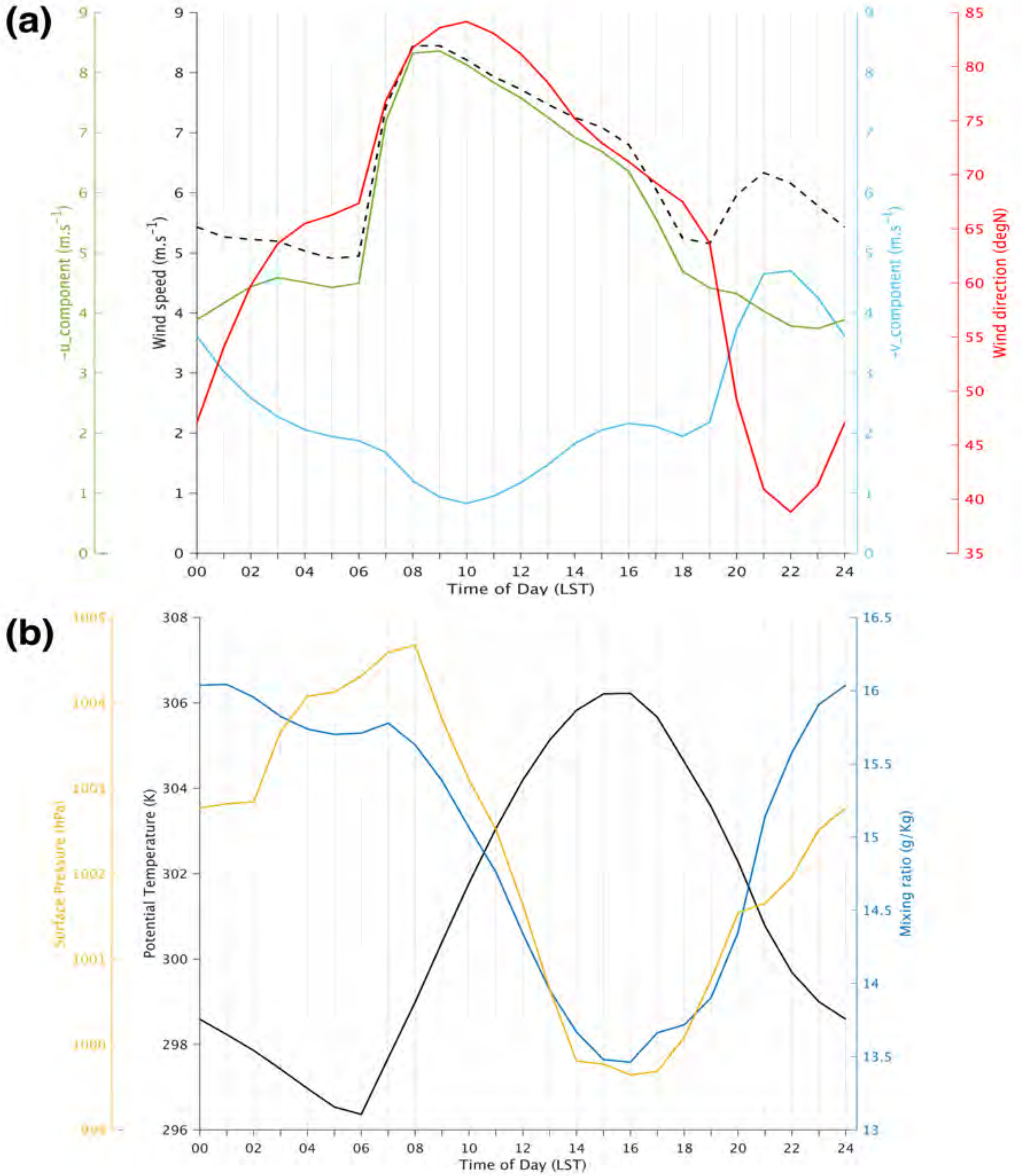

Figure 3.9: Diurnal cycle of (a) wind direction (red, degN), wind speed (dashed, m s^{-1}), zonal wind speed (green, m s^{-1}), meridional wind speed (cyan, m s^{-1}), and (b) surface pressure (yellow, hPa), potential temperature (black, K), and mixing ratio content (blue, g kg^{-1}), from November 2013–March 2014, at a selected surface location (8ºN– 66.5ºW; Aguaro-Guariquito national park, Venezuela) along the axis of propagation L (Fig. 3.5). The zonal and meridional wind speeds are negative (easterly and northerly components, respectively).

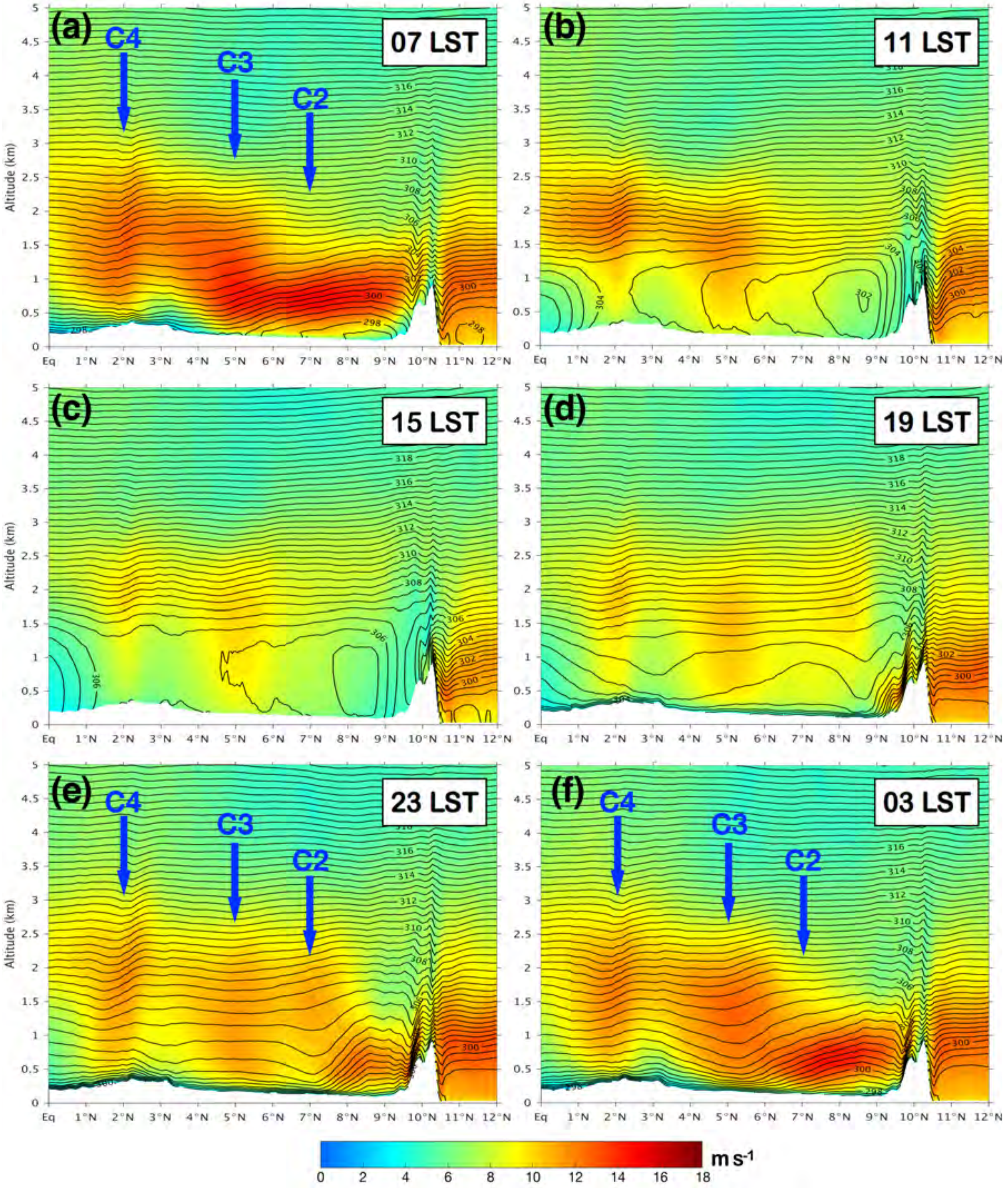

Figure 3.10: Diurnal variation of mean wind speed (shaded, m s^{-1}) and potential temperature (contoured, K), from November 2013–March 2014, in a vertical cross-section along the axis of propagation K (Fig. 3.5) at: (a) 0700 LST, (b) 1100 LST, (c) 1500 LST, (d) 1900 LST, (e) 2300 LST, (f) 0300 LST. The relative positions of the C2–C4 cores are also shown. Potential temperatures are contoured in 0.5 K increments.

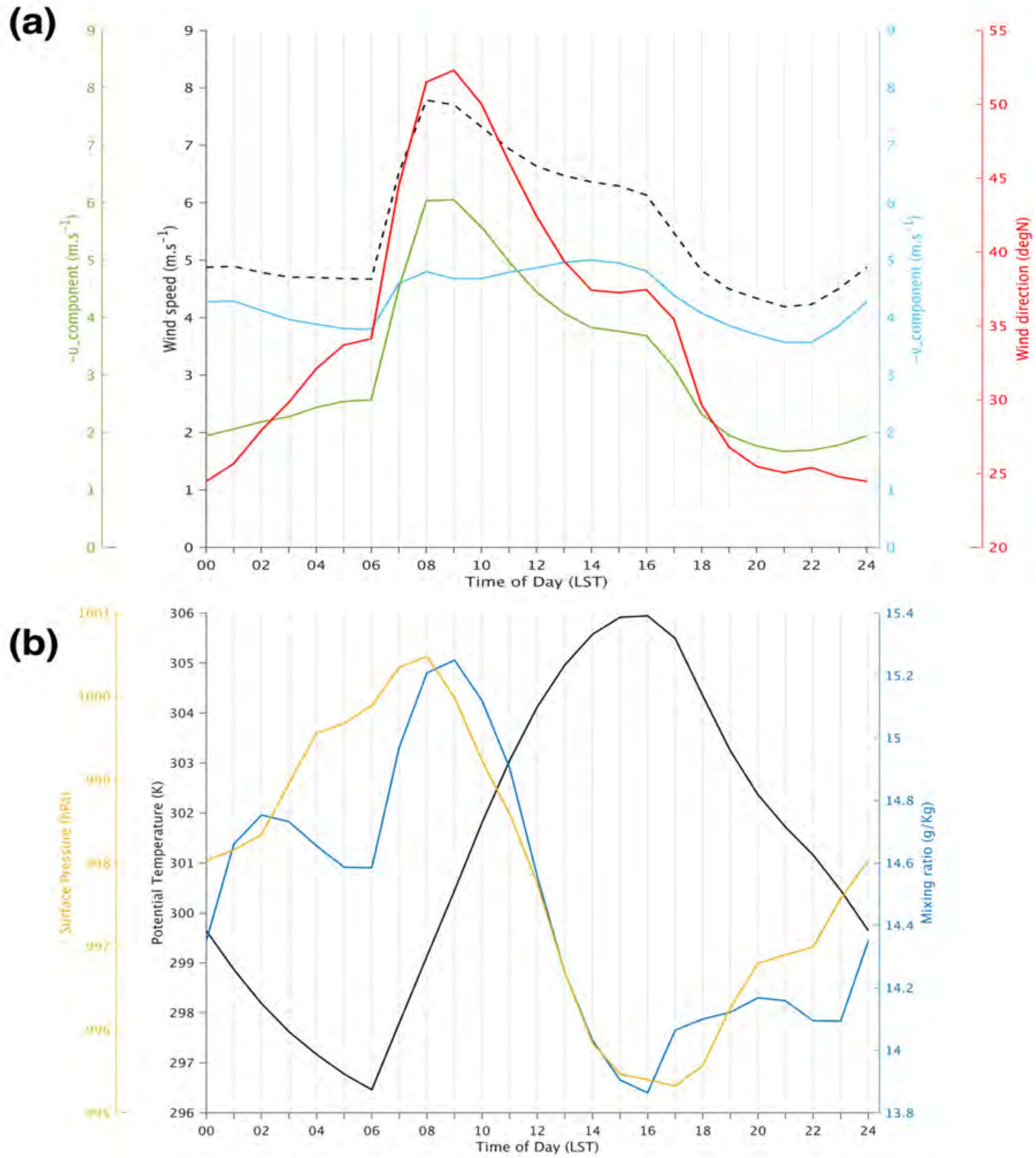

Figure 3.11: Diurnal cycle of (a) wind direction (red, degN), wind speed (dashed, m s^{-1}), zonal wind speed (green, m s^{-1}), meridional wind speed (cyan, m s^{-1}), and (b) surface pressure (yellow, hPa), potential temperature (black, K), and mixing ratio content (blue, g kg^{-1}), from November 2013–March 2014, at a selected surface location (7.5ºN– 69.7ºW; Las Mulas, Apure-Venezuela) along the axis of propagation K (Fig. 3.5). The zonal and meridional wind speeds are negative (easterly and northerly components, respectively).

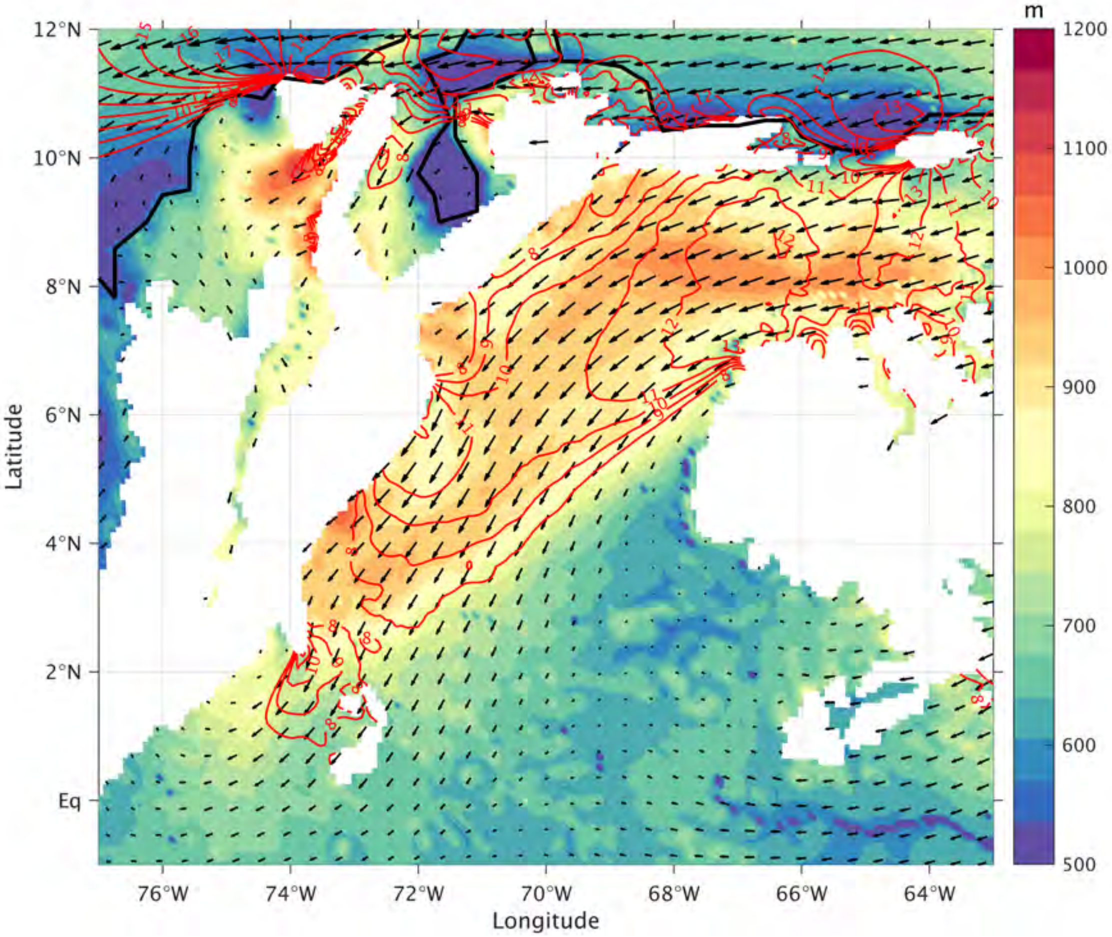

Figure 3.12: Horizontal characterization of mean diurnal PBL height (shaded, m AGL) and mean wind field during November 2013–March 2014. Isotachs (red, m s^{-1}) and velocity vectors at 500 m AGL. Wind speeds greater than 8 m s^{-1} are contoured in 1 m s^{-1} increments.

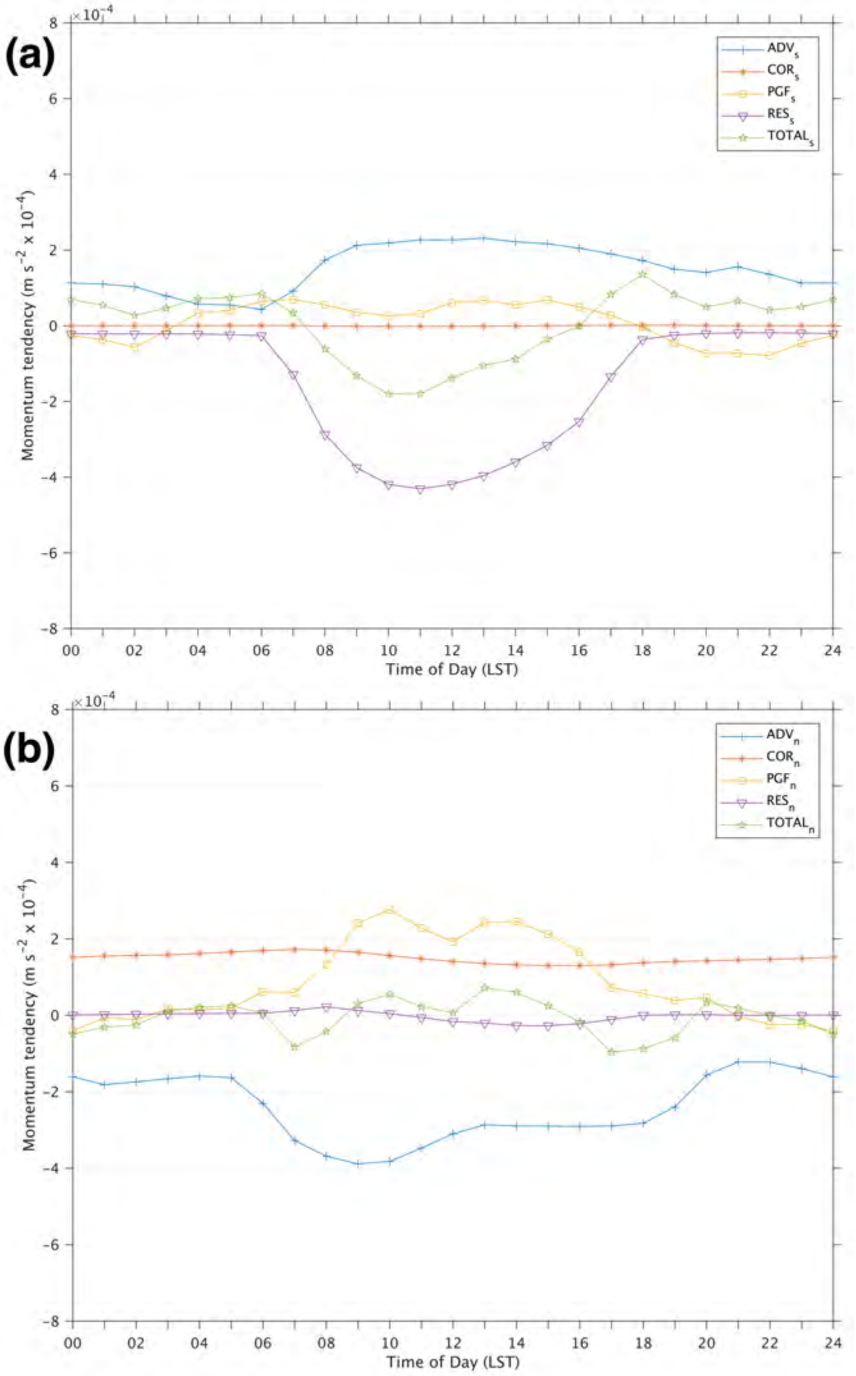

Figure 3.13: Diurnal cycle of the 950–800-hPa-mean (a) streamwise (s) and (b) crosswise (n) momentum balance components at the C3 region near sloping terrain (~5ºN–72.5ºW) during November 2013–March 2014. The advection (blue crosses), Coriolis (red asterisks), PGF (yellow squares), residual (purple triangles), and total (green stars) tendency terms in m $s^{-2} \times 10^{-4}$.

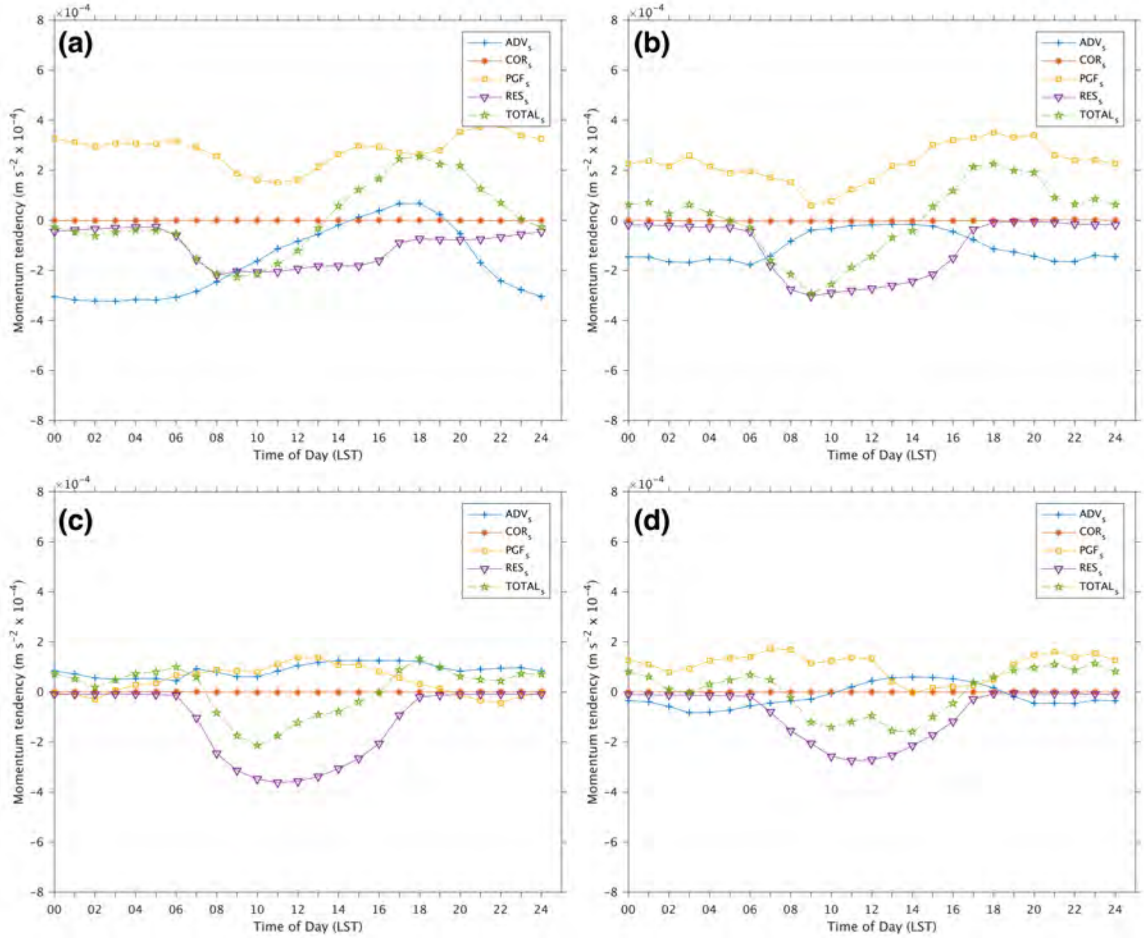

Figure 3.14: Diurnal cycle of the 950–800-hPa-mean streamwise momentum balance component during November 2013–March 2014 at (a) C1, (b) C2, (c) C3, and (d) C4 regions. The advection (blue crosses), Coriolis (red asterisks), PGF (yellow squares), residual (purple triangles), and total (green stars) tendency terms in m s^{-2} × 10^{-4}.

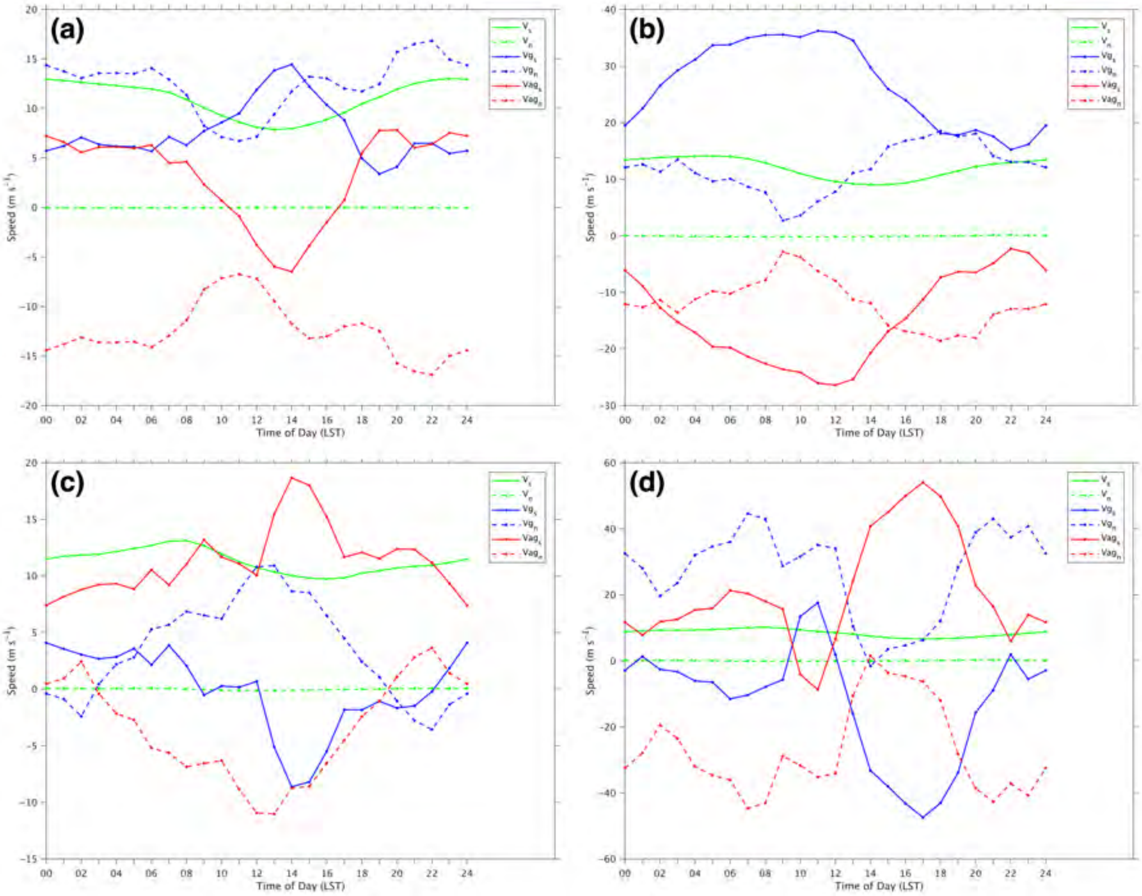

Figure 3.15: Diurnal cycle of the 950–800-hPa-mean streamwise (s) and crosswise (n) horizontal (green), geostrophic (blue), and ageostrophic (red) winds (m s^{-1}) during November 2013–March 2014 at (a) C1, (b) C2, (c) C3, and (d) C4 regions. Streamwise components in solid lines and crosswise components dashed. Geostrophic and ageostrophic crosswise components balance around zero m s^{-1} due to the rotated coordinate system.

Chapter 4

Summary and Conclusions

In this study, the dynamical downscaling from November 2013–March 2014 of the large-scale atmospheric conditions provided by the 0.5º x 0.5º GFS Analysis, developed high-resolution detail of the spatial structure and evolution of the Orinoco low-level jet (OLLJ), which flows over the flatlands between the Andes Cordillera and the Guiana Highlands. The finer spatial and temporal characterizations of the OLLJ—at least three times more than in previous studies—obtained through the advanced-research version of the Weather Research and Forecasting (WRF) model, indicate that:

(a) the OLLJ is present from the Orinoco Delta in Venezuela to the Amazon forest in Colombia, as a single stream tube (2000 km long × 300 km wide × 3 km deep, approximately) with mean wind speeds greater than 8 m s^{-1};

(b) the flow interaction with the surrounding topography produces four localized low-level jet streaks (LLJSs; i.e., the regions with maximum mean wind speeds at the Guanipa Mesa, Guiana Highlands, Eastern Cordillera, and Macarena mountain range) along its curved axis of propagation;

(c) the core mean heights at the entrance, mid-corridor, and exit regions (750 m AGL, 1200 m AGL, and 1500 m AGL) differ under the influence of the sloped terrain; and

(d) because of being ten times wider than deep, the OLLJ has an ellipsoidal vertical shape.

The OLLJ is present from November to March, displaying the least monthly wind speed (~9 m s^{-1}) in November and the greatest spatial reduction (~1500 km in length) in March, whereas its greatest monthly wind speed (~13 m s^{-1}) and longest and widest extension (2100 km × 400 km) occur in January. The intraseasonal variability of the wind speed and potential temperature only has significant periodicity in the diurnal and semidiurnal scales, with no other meaningful cycles evident during the Austral summer.

In general, during the diurnal cycle, the OLLJ exhibits maxima mean wind speeds (13–17 m s^{-1}) early in the morning, when potential temperatures in the 950–800-hPa layer are the lowest, and minima mean wind speeds (~8–9 m s^{-1}) in the afternoon, when potential temperatures in the layer are the highest. However, the maxima mean wind speeds at each core location (C1–C4) occur at different times (2300, 0400, 0700, 0900 LST, respectively), thus showing an acceleration of the wind in the direction of the OLLJ propagation.

The momentum balance analysis performed in a streamwise- and crosswise-rotated coordinate system showed that the streamwise acceleration of the wind is not uniform across the domain, as it was somewhat expected from consideration of the inertial oscillation and topographic thermal forcing mechanisms. Consequently, it was established that the OLLJ is the result of four phenomena acting together to accelerate the wind over the valley of the Orinoco River basin, namely:

1) the sea breeze penetration over the Orinoco River delta and Unare River depression,
2) katabatic flow down the Coastal Cordillera,
3) three expansion fans from point wakes in the topography, and
4) diurnal variation of turbulent diffusivity.

The continuous nocturnal advection of relatively cool air through the Orinoco delta region, Unare River depression (i.e., sea breezes penetration), and downslope the Coastal Cordillera (katabatic flow), constitute a single density current that merges over the Llanos and propagates up-valley, causing acceleration of the wind behind its leading edge. Before combining over the Llanos, the Orinoco Delta sea breeze generates the first LLJS (C1) as the advected cool maritime air flows downslope the western limits of the Guanipa Mesa. Thereafter, as the merged density current and large-scale flow move along the Orinoco River basin, the interaction with surrounding topography generates the other LLJSs (C2–C4) from the expansion fans produced by point wakes at three fixed locations: the Guiana Highlands, Eastern Cordillera, and Macarena mountain range. Supercritical-channel-flow theory supports the generation of these expansion fans and reasonably predicts their final wind speeds and PBL heights.

Additionally, the diurnal variation of turbulent diffusivity acts to decelerate (day) and accelerate (night) the horizontal winds across the domain, triggering the inertial oscillation mechanism and causing the clockwise rotation of the wind. However, opposite to what happens in higher latitudes, the role of the diurnal variation of turbulent diffusivity in the OLLJ formation is secondary, given that the maxima wind speeds as the result of combined geostrophic and ageostrophic winds occur in only two of the four cores. These results suggest that LLJs near the equator may originate from different phenomena besides the traditional inertial oscillation and topographic thermal forcing mechanisms.

Compared against the results from previous authors, dynamical downscaling is demonstrated to be an effective method to better resolve the horizontal and vertical characteristics of the OLLJ, not only improving its diurnal and austral-summer evolution, and identification and location of LLJSs inside the stream tube, but also in determining the mechanisms leading to its formation; assessment that has not previously been undertaken.

The advancements achieved in this research set up the initial foundation for the development of practical applications of the OLLJ in wind energy generation, aviation safety, fire weather prediction, oil-extraction pollutants transport, and public health, among others.

Appendix A

OLLJ-3D Austral Summer and Diurnal Evolution

The figures in this appendix provide a 3D visualization of the complex topography in northern South America and the evolution of the OLLJ average structure, during the Austral summer (Fig. A1) and in a 24-h cycle (Fig. A2). Because of the presence of the Caribbean low-level jet, the wind-speed stream tubes north of 10ºN have been filter out to improve clarity.

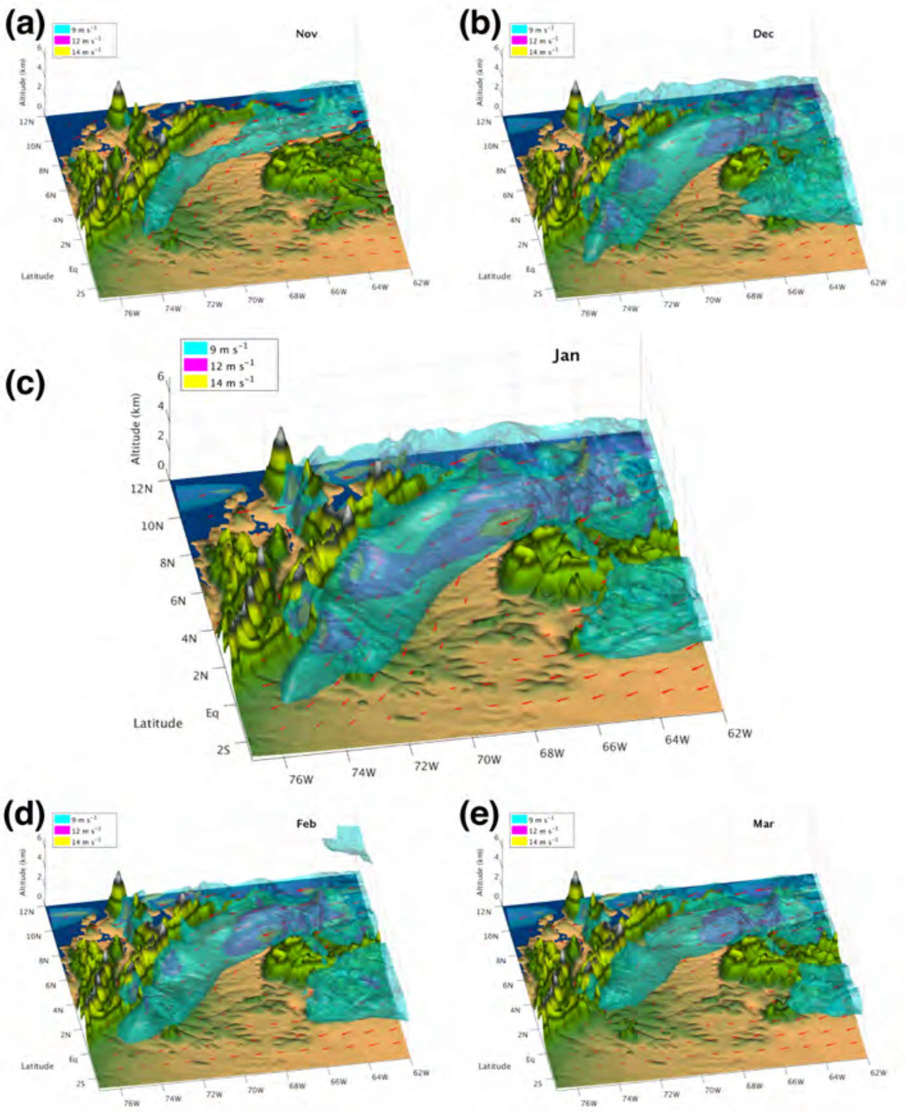

Figure A1: Austral summer evolution of the Orinoco low-level jet in 3D, showing monthly mean wind-speed stream tubes of 9 m s^{-1} (cyan), 12 m s^{-1} (magenta) and 14 m s^{-1} during (a) November, (b) December, (c) January, (d) February, and (e) March. Wind vectors at 900 m AGL are shown in red.

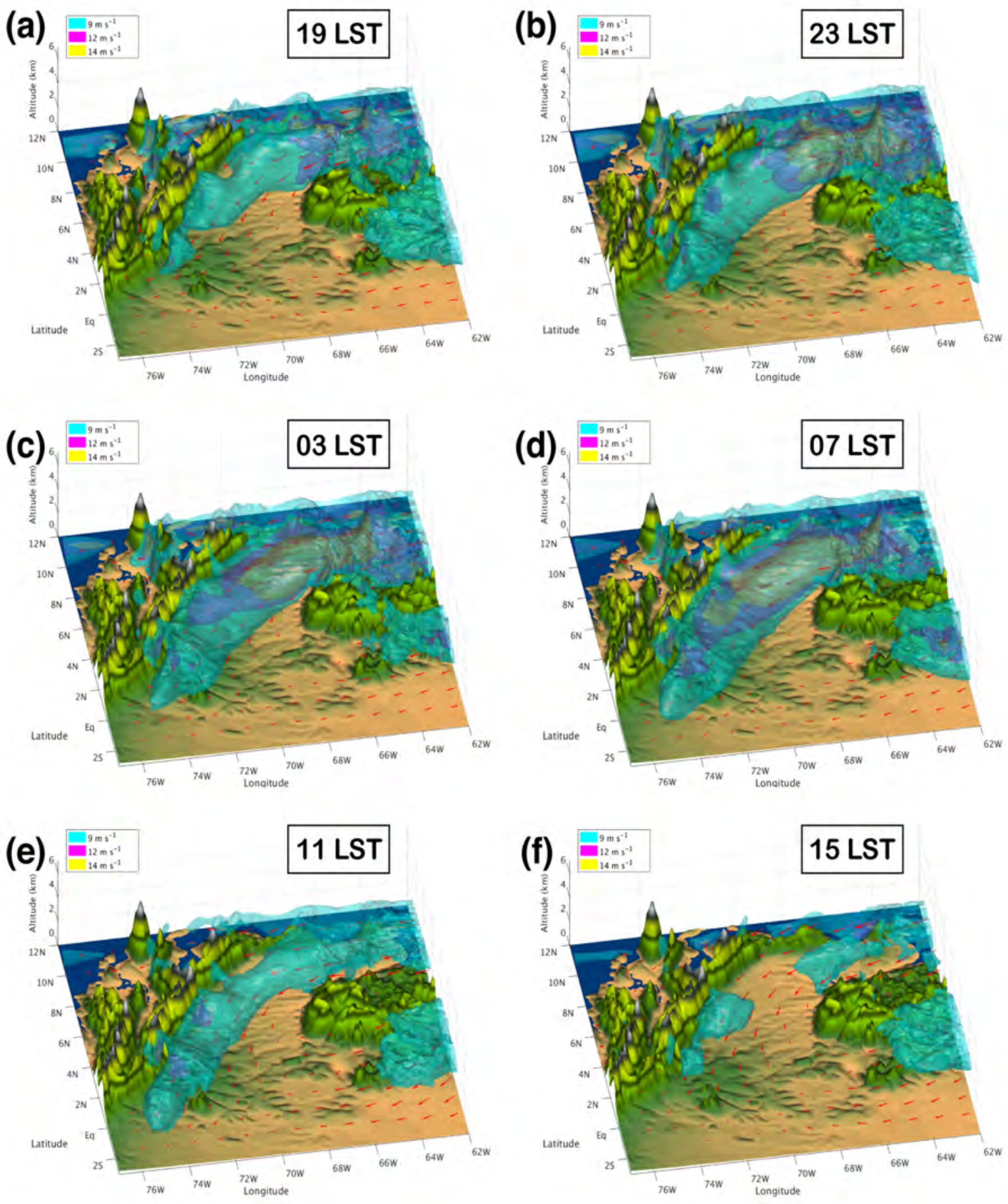

Figure A2: Diurnal evolution of the Orinoco low-level jet in 3D, showing hourly mean wind-speed stream tubes of 9 m s^{-1} (cyan), 12 m s^{-1} (magenta) and 14 m s^{-1} at (a) 1900 LST, (b) 2300 LST, (c) 0300 LST, (d) 0700 LST, (e) 1100 LST, and (f) 1500 LST. Wind vectors at 900 m AGL are shown in red.

Appendix B

Supercritical-Channel-Flow Hydraulic Theory Uncertainty Estimation

The uncertainties in the calculations presented in section 3.3.3 and Table 3.2 are estimated as follows. The total uncertainty, δq, of a function $q(x, \dots, z)$ for which the uncertainties in $x, \dots, z$ are $\delta x, \dots, \delta z$, respectively, is estimated via Taylor (1997) as

$$\delta q = \sqrt{\left(\frac{\partial q}{\partial x}\delta x\right)^2 + \cdots + \left(\frac{\partial q}{\partial z}\delta z\right)^2} \tag{B1}$$

In the supercritical-channel-flow cases analyzed in Chapter 3, upstream wind speed and PBL height, lower-troposphere static stability, and the angular change in the flow direction due to the bending boundary (Figs. 3.6, 3.8, 3.10, and 3.12) are obtained from visual inspection of the respective fields and determine Fr and $d\theta$, along with their corresponding uncertainties. For instance, using Eq. (B1), the total uncertainty in the Froude Number (δFr) upstream of the Guiana Highland expansion fan is given by

$$\delta Fr = \sqrt{\left(\frac{\partial Fr}{\partial U}\delta U\right)^2 + \left(\frac{\partial Fr}{\partial g'}\delta g'\right)^2 + \left(\frac{\partial Fr}{\partial h}\delta h\right)^2} \tag{B2}$$

$$\delta Fr = 0.22$$

so that $Fr = 1.32 \pm 0.22$.

The measured values and uncertainties of Fr and $d\theta$ propagate through the subsequent calculations in Eqs. (4)–(7). The total uncertainty for every new variable is obtained using Eq. (B1), with the exception of $\delta\beta$ in Eq. (4), where β is a function of Fr only, for which a simpler formula can be used:

$$\delta\beta = \left|\frac{d\beta}{dFr}\right| \delta Fr \tag{B3}$$

Table 3.2 summarizes the predicted final wind speeds, PBL heights, and the corresponding uncertainties for each expansion fan.

References

Amador, J. A., 2008: The Intra-Americas Sea low-level jet: Overview and future research. *Ann. N. Y. Acad. Sci.*, **1146**, 153–188, doi:10.1196/annals.1446.012. http://doi.wiley.com/10.1196/annals.1446.012 (Accessed July 16, 2018).

Archer, C. L., L. Delle Monache, and D. L. Rife, 2014: Airborne wind energy: Optimal locations and variability. *Renew. Energy*, **64**, 180–186, doi:10.1016/j.renene.2013.10.044. http://dx.doi.org/10.1016/j.renene.2013.10.044.

Balmez, M., and S. Ştefan, 2014: On the Formation Mechanism of Low-Level Jet Over Bucharest's Airports. *Atmos. Phys.*, **59**, 792–807.

Banta, R. M., and Coauthors, 1998: Daytime buildup and nighttime transport of urban ozone in the boundary layer during a stagnation episode. *J. Geophys. Res. Atmos.*, **103**, 22519, doi:10.1029/98JD01020.

——, L. S. Darby, J. D. Fast, J. O. Pinto, C. D. Whiteman, W. J. Shaw, and B. W. Orr, 2004: Nocturnal Low-Level Jet in a Mountain Basin Complex. Part I: Evolution and Effects on Local Flows. *J. Appl. Meteorol.*, **43**, 1348–1365, doi:10.1175/JAM2142.1. http://journals.ametsoc.org/doi/abs/10.1175/JAM2142.1.

——, Y. L. Pichugina, and W. A. Brewer, 2006: Turbulent Velocity-Variance Profiles in the Stable Boundary Layer Generated by a Nocturnal Low-Level Jet. *J. Atmos. Sci.*, **63**, 2700–2719, doi:10.1175/JAS3776.1.

Blackadar, A. K., 1957: Boundary layer wind maxima and their significance for the growth of nocturnal inversions. *Bull. Am. Meteorol. Soc.*, **38**, 283–290.

Bonner, W. D., 1963: Thunderstorms and the low-level jets. 19–33.

——, 1968: Climatology of the Low Level Jet. *Mon. Weather Rev.*, **96**, 833–850, doi:10.1175/1520-0493(1968)096<0833:COTLLJ>2.0.CO;2.

——, and J. Paegle, 1970: Diurnal variations in boundary layer winds over the south-central united states in summer. *Mon. Weather Rev.*, **98**, 735–744, doi:10.1175/1520-0493(1970)098<0735:DVIBLW>2.3.CO;2.

Chen, F., and J. Dudhia, 2001: Coupling and advanced land surface-hydrology model with the Penn State-NCAR MM5 modeling system. Part I: Model implementation and sensitivity. *Mon. Weather Rev.*, **129**, 569–585, doi:10.1175/1520-0493(2001)129<0569:caalsh>2.0.co;2.

Chen, G. T.-J., and Y.-S. Hsu, 1997: Composite structure of a Low-Level Jet over Southern China observed during the TAMEX period. *J. Meteorol. Soc. Japan*, **75**, 1003–1018.

Chen, R., and L. Tomassini, 2015: The Role of Moisture in Summertime Low-Level Jet Formation and Associated Rainfall over the East Asian Monsoon Region. *J. Atmos. Sci.*, **72**, 3871–3890, doi:10.1175/JAS-D-15-0064.1. http://journals.ametsoc.org /doi/10.1175/JAS-D-15-0064.1.

Clarke, R. H., R. K. Smith, and D. G. Reid, 1981: The Morning Glory of the Gulf of Carpentaria: An Atmospheric Undular Bore. *Mon. Weather Rev.*, **109**, 1726–1750, doi:10.1175/1520-0493(1981)109<1726:TMGOTG>2.0.CO;2. http://journals.ametsoc.org/doi/abs/10.1175/1520-0493%281981%29109%3C1726%3ATMGOTG%3E2.0.CO%3B2.

Coleman, T. A., K. R. Knupp, and D. E. Herzmann, 2010: An undular bore and gravity waves illustrated by dramatic time-lapse photography. *J. Atmos. Ocean. Technol.*, 1355–1361, doi:10.1175/2010JTECHA1472.1.

Cook, K. H., and E. K. Vizy, 2010: Hydrodynamics of the Caribbean low-level jet and its relationship to precipitation. *J. Clim.*, **23**, 1477–1494, doi:10.1175/2009JCLI3210.1.

Darby, L. S., K. J. Allwine, and R. M. Banta, 2006: Nocturnal low-level jet in a mountain basin complex. Part II: Transport and diffusion of tracer under stable conditions. *J. Appl. Meteorol. Climatol.*, **45**, 740–753, doi:10.1175/JAM2367.1.

Douglas, M., J. Murillo, and J. Mejia, 2005: Conducting short duration field programs to evaluate sounding site representativeness and potential climate monitoring biases. Examining the low-level jet over the Venezuelan llanos during the 2005 dry season. *15th Conference on Applied Climatology*, Savannah, GA http://www.nssl.noaa.gov/projects/pacs.

Doyle, J. D., and T. T. Warner, 1993: A three-dimensional numerical investigation of a Carolina Coastal Low-Level Jet during GALE IOP 2. *Mon. Weather Rev.*, **121**, 1030–1047, doi:10.1175/1520-0493(1993)121<1030:ATDNIO>2.0.CO;2. http://journals.ametsoc.org/doi/abs/10.1175/1520-0493(1993)121%3C1030:ATDNIO%3E2.0.CO;2.

Du, Y., and R. Rotunno, 2014: A Simple Analytical Model of the Nocturnal Low-Level Jet over the Great Plains of the United States. *J. Atmos. Sci.*, **71**, 3674–3683, doi:10.1175/JAS-D-14-0060.1. http://journals.ametsoc.org/doi/abs/10.1175/JAS-D-14-0060.1.

——, Q. Zhang, Y. L. Chen, Y. Zhao, and X. Wang, 2014: Numerical simulations of spatial distributions and diurnal variations of low-level jets in China during early summer. *J. Clim.*, **27**, 5747–5767, doi:10.1175/JCLI-D-13-00571.1.

——, Y.-L. Chen, and Q. Zhang, 2015a: Numerical Simulations of the Boundary Layer Jet off the Southeastern Coast of China. *Mon. Weather Rev.*, **143**, 1212–1231, doi:10.1175/MWR-D-14-00348.1. http://journals.ametsoc.org/doi/10.1175/MWR-D-

14-00348.1.

——, R. Rotunno, and Q. Zhang, 2015b: Analysis of WRF-Simulated Diurnal Boundary Layer Winds in Eastern China Using a Simple 1D Model. *J. Atmos. Sci.*, **72**, 714–727, doi:10.1175/JAS-D-14-0186.1. http://journals.ametsoc.org/doi/10.1175/JAS-D-14-0186.1.

Fedorovich, E., J. A. Gibbs, and A. Shapiro, 2017: Numerical Study of Nocturnal Low-Level Jets over Gently Sloping Terrain. *J. Atmos. Sci.*, **74**, 2813–2834, doi:10.1175/JAS-D-17-0013.1. http://journals.ametsoc.org/doi/10.1175/JAS-D-17-0013.1.

Findlater, J., 1969: A major low level air current near the Indian Ocean during the northern summer. *Q. J. R. Meteorol. Soc.*, **95**, 362–380.

Foghin-Pillin, S., 2016: Evidencias de la penetración de brisas de mar en la depresión del río Unare y Llanos de Anzoátegui. *Rev. Invest. (Guadalajara).*, **40**, 39–62.

Fromm, M. D., and R. Servranckx, 2003: Transport of forest fire smoke above the tropopause by supercell convection. *Geophys. Res. Lett.*, **30**, 1542, doi:10.1029/2002GL016820. http://doi.wiley.com/10.1029/2002GL016820.

Giannakopoulou, E. M., and R. Toumi, 2012: The Persian Gulf summertime low-level jet over sloping terrain. *Q. J. R. Meteorol. Soc.*, **138**, 145–157, doi:10.1002/qj.901.

Gilford, M. T., R. C. Bonam, D. L. Martens, G. Myles, and M. J. Vojtesak, 1992: *South America South of the Amazon River – A Climatological Study*. USAF Environmental Technical Applications Center, Scott Air Force Base, Illinois, USA, 692 pp.

Golding, W. L., 2005: Low-Level Windshear and Its Impact on Airlines. *J. Aviat. Educ. Res.*, **14**, doi:10.15394/jaaer.2005.1530. http://commons.erau.edu/jaaer/vol14/iss2/8/.

Goler, R. A., and M. J. Reeder, 2004: The Generation of the Morning Glory. 1360–1376.

Guan, W.-L., and K. Yong, 2002: Review of Aviation Accidents Caused by Wind Shear and Identification Methods. *J. Chinese Soc. Mech. Eng.*, **23**, 99–109. papers2://publication/uuid/55540006-3DA0-4B07-919C-AF6B195EAD7E.

Haase, S. P., and R. K. Smith, 1989: The numerical simulation of atmospheric gravity currents. Part II: Environments with stable layers. *Geophys. Astrophys. Fluid Dyn.*, **46**, 35–51.

Hart, J. E., 1977: On the theory of the East African Low Level Jet Stream. *Pure Appl. Geophys. PAGEOPH*, **115**, 1263–1282, doi:10.1007/BF00874409. http://link.springer.com/10.1007/BF00874409.

Hastenrath, S., 1991: *Climate dynamics of the tropics*. Springer Science+Business Media Dordrecht, 488 pp. http://link.springer.com/10.1007/978-94-011-3156-8.

He, M.-Y., H. B. Liu, B. Wang, and D. L. Zhang, 2016: A modeling study of a low-level jet along the Yun-Gui Plateau in South China. *J. Appl. Meteorol. Climatol.*, **55**, 41–60, doi:10.1175/JAMC-D-15-0067.1.

Hidalgo, H. G., A. M. Durán-Quesada, J. A. Amador, and E. J. Alfaro, 2015: The caribbean low-level jet, the inter-tropical convergence zone and precipitation patterns in the intra-Americas Sea: A proposed dynamical mechanism. *Geogr. Ann. Ser. A Phys. Geogr.*, **97**, 41–59, doi:10.1111/geoa.12085.

Holton, J. R., 1967: The diurnal boundary layer wind oscillation above sloping terrain. *Tellus*, **19**, 199–205, doi:10.3402/tellusa.v19i2.9766. http://tellusa.net/index.php/tellusa/article/view/9766.

Iacono, M. J., J. S. Delamere, E. J. Mlawer, M. W. Shephard, S. A. Clough, and W. D. Collins, 2008: Radiative forcing by long-lived greenhouse gases: Calculations with the AER radiative transfer models. *J. Geophys. Res. Atmos.*, **113**, 2–9, doi:10.1029/2008JD009944.

International Civil Aviation Organization, 2005: *Manual on low-level wind shear*. 1. ed. Internat. Civil Aviation Organization, Montréal, 7 pp.

Juliano, T. W., T. R. Parish, D. A. Rahn, and D. C. Leon, 2017: An atmospheric hydraulic jump in the Santa Barbara Channel. *J. Appl. Meteorol. Climatol.*, 2981–2999, doi:10.1175/JAMC-D-16-0396.1.

Kain, J. S., 2004: The Kain–Fritsch Convective Parameterization: An Update. *J. Appl. Meteorol.*, **43**, 170–181, doi:10.1175/1520-0450(2004)043<0170:TKCPAU>2.0.CO;2. http://journals.ametsoc.org/doi/abs/10.1175/1520-0450%282004%29043%3C0170%3ATKCPAU%3E2.0.CO%3B2.

Koch, S. E., and W. L. Clark, 1999: A Nonclassical Cold Front Observed during COPS-91: Frontal Structure and the Process of Severe Storm Initiation. *J. Atmos. Sci.*, **56**, 2862–2890, doi:10.1175/1520-0469(1999)056<2862:ANCFOD>2.0.CO;2. http://journals.ametsoc.org/doi/abs/10.1175/1520-0469%281999%29056%3C2862%3AANCFOD%3E2.0.CO%3B2 (Accessed July 16, 2018).

——, M. Pagowski, J. W. Wilson, F. Fabry, C. Flamant, W. Feltz, G. Schwemmer, and B. Geerts, 2005: The Structure and Dynamics of Atmospheric Bores and Solitons and Modeling Experiments during IHOP. *11th Conference on Mesoscale Processes and the 32nd Conference on Radar Meteorology*, 14.

Krishnamurthy, L., G. A. Vecchi, R. Msadek, A. Wittenberg, T. L. Delworth, and F. Zeng, 2015: The seasonality of the great plains low-level Jet and ENSO relationship. *J. Clim.*, **28**, 4525–4544, doi:10.1175/JCLI-D-14-00590.1.

Kulesa, G., 2002: Weather and Aviation: How Does Weather Affect the Safety and

Operations of Airports and Aviation, and How Does FAA Work to Manage Weather-related Effects? *The Potential Impacts of Climate Change on Transportation Workshop*, Washington DC, USDOT Center for Climate Change and Environmental Forecasting, 1–10.

Labar, R. J., M. Douglas, J. Murillo, and J. F. Mejia, 2005: The Llanos Low-Level Jet and its Association with Venezuelan Convective Precipitation. *Weather*, **98926**, 1–21.

Liechti, F., and E. Schaller, 1999: The use of low-level jets by migrating birds. *Naturwissenschaften*, **86**, 549–551, doi:10.1007/s001140050673.

Lindzen, R. S., and S. Chapman, 1969: Atmospheric tides. *Space Sci. Rev.*, **10**, 3–188.

Liu, H., M.-Y. He, B. Wang, and Q. Zhang, 2014: Advances in low-level jet research and future prospects. *J. Meteorol. Res.*, **28**, 57–75, doi:10.1007/s13351-014-3166-8.

Liu, M., D. L. Westphal, T. R. Holt, and Q. Xu, 2000: Numerical Simulation of a Low-Level Jet over Complex Terrain in Southern Iran. *Mon. Weather Rev.*, **128**, 1309–1327, doi:10.1175/1520-0493(2000)128<1309:NSOALL>2.0.CO;2.

Lo, J. C.-F., Z.-L. Yang, and R. A. Pielke, 2008: Assessment of three dynamical climate downscaling methods using the Weather Research and Forecasting (WRF) model. *J. Geophys. Res.*, **113**, D09112, doi:10.1029/2007JD009216. http://doi.wiley.com/10.1029/2007JD009216.

Maldonado, T., A. Rutgersson, J. Amador, E. Alfaro, and B. Claremar, 2016: Variability of the Caribbean low-level jet during boreal winter: Large-scale forcings. *Int. J. Climatol.*, **36**, 1954–1969, doi:10.1002/joc.4472. http://doi.wiley.com/10.1002/joc.4472 (Accessed July 16, 2018).

——, ——, R. Caballero, F. S. R. Pausata, E. Alfaro, and J. Amador, 2017: The role of the meridional sea surface temperature gradient in controlling the Caribbean low-level jet. *J. Geophys. Res. Atmos.*, **122**, 5903–5916, doi:10.1002/2016JD026025. http://doi.wiley.com/10.1002/2016JD026025 (Accessed July 16, 2018).

Marengo, J. A., W. R. Soares, C. Saulo, and M. Nicolini, 2004: Climatology of the low-level jet east of the Andes as derived from the NCEP-NCAR reanalyses: Characteristics and temporal variability. *J. Clim.*, **17**, 2261–2280, doi:10.1175/1520-0442(2004)017<2261:COTLJE>2.0.CO;2.

Markowski, P., and Y. Richardson, 2010: The nocturnal low-level wind maximum. *Mesoscale meteorology in midlatitudes*, Wiley-Blackwell, Chichester, UK, 105–112.

Mlawer, E. J., S. J. Taubman, P. D. Brown, M. J. Iacono, and S. A. Clough, 1997: Radiative transfer for inhomogeneous atmospheres: RRTM, a validated correlated-k model for the longwave. *J. Geophys. Res. Atmos.*, **102**, 16663–16682, doi:10.1029/97JD00237. http://doi.wiley.com/10.1029/97JD00237.

Moisseeva, N., and D. G. Steyn, 2014: Dynamical analysis of sea-breeze hodograph rotation in Sardinia. *Atmos. Chem. Phys.*, **14**, 13471–13481, doi:10.5194/acp-14-13471-2014; 10.5194/acp-14-13471-2014-supplement.

Montoya, G. J., J. Pelkowski, and J. Eslava, 2001: Sobre los alisios del nordeste y la existencia de una corriente en el piedemonte oriental Andino. *Rev. Acad. Colomb. Cienc*, **25**, 363–370, doi:0370-3908.

Muñoz, E., A. J. Busalacchi, S. Nigam, and A. Ruiz-Barradas, 2008: Winter and summer structure of the Caribbean low-level jet. *J. Clim.*, **21**, 1260–1276, doi:10.1175/2007JCLI1855.1.

Nakanishi, M., and H. Niino, 2006: An improved Mellor-Yamada Level-3 model: Its numerical stability and application to a regional prediction of advection fog. *Boundary-Layer Meteorol.*, **119**, 397–407, doi:10.1007/s10546-005-9030-8.

Do Nascimento, M. G., D. L. Herdies, and D. O. De Souza, 2016: The south American water balance: The influence of low-level jets. *J. Clim.*, **29**, 1429–1449, doi:10.1175/JCLI-D-15-0065.1.

Nicholson, S., 2016: The Turkana low-level jet: Mean climatology and association with regional aridity. *Int. J. Climatol.*, **36**, 2598–2614, doi:10.1002/joc.4515. http://doi.wiley.com/10.1002/joc.4515 (Accessed July 16, 2018).

Olson, D. M., and E. Dinerstein, 2002: The Global 200: Priority Ecoregions for Global Conservation. *Ann. Missouri Bot. Gard.*, **89**, 199–224, doi:10.2307/3298564. http://www.jstor.org/stable/3298564?origin=crossref.

Outten, S. D., I. A. Renfrew, and G. N. Petersen, 2009: An easterly tip jet off Cape Farewell, Greenland. II: Simulations and dynamics. *Q. J. R. Meteorol. Soc.*, **135**, 1934–1949, doi:10.1002/qj.531.

Parish, T. R., 2017: On the Forcing of the Summertime Great Plains Low-Level Jet. *J. Atmos. Sci.*, **74**, 3937–3953, doi:10.1175/JAS-D-17-0059.1. http://journals.ametsoc.org/doi/10.1175/JAS-D-17-0059.1.

Patricola, C. M., and P. Chang, 2017: Structure and dynamics of the Benguela low-level coastal jet. *Clim. Dyn.*, **49**, 2765–2788, doi:10.1007/s00382-016-3479-7.

Percival, D. B., and A. T. Walden, 1993: *Spectral Analysis for Physical Applications: Multitaper and Conventional Univariate Techniques*. Cambridge University Press, Cambridge, New York, NY, USA, 583 pp.

Petroliagkis, T., G. Liberta, T. Artes, D. Rodriguez-Aseretto, M. Di Leo, and J. San-Miguel-Ayanz, 2015: Stability of atmospheric flow and low-level jets influencing forest fire behavior - An EFFIS report. *EUR – Scientific and Technical Research series*, Vol. EUR 27362 of, Publications Office of the European Union, Luxembourg,

p. 30 http://dx.doi.org/10.2788/54976.

Poveda, G., and O. Mesa, 1999: La Corriente de chorro superficial del oeste ("del Chocó") y otras dos corrientes de chorro en Colombia: Climatología y Variabilidad durante las fases del ENSO. *Rev. Acad. Colomb. Cienc*, **23**, 517–528.

Poveda, G., and O. J. Mesa, 2000: On the Existence of Lloro (the Rainiest Locality on Earth): Enhanced Ocean-Land-Atmosphere Interaction by a Low- Level Jet. *Geophys. Res. Lett.*, **27**, 1675–1678.

——, L. Jaramillo, and L. F. Vallejo, 2014: Seasonal precipitation patterns along pathways of South American low-level jets and aerial rivers. *Water Resour. Res.*, **50**, 98–118, doi:10.1002/2013WR014087. http://doi.wiley.com/10.1002/2013WR014087 (Accessed July 16, 2018).

Prabha, T. V., B. N. Goswami, B. S. Murthy, and J. R. Kulkarni, 2011: Nocturnal low-level jet and "atmospheric streams" over the rain shadow region of indian western ghats. *Q. J. R. Meteorol. Soc.*, **137**, 1273–1287, doi:10.1002/qj.818.

Ranjha, R., G. Svensson, M. TjernströM, and A. Semedo, 2013: Global distribution and seasonal variability of coastal low-level jets derived from ERA-Interim reanalysis. *Tellus A Dyn. Meteorol. Oceanogr.*, **65**, 1–21, doi:10.3402/tellusa.v65i0.20412.

Reeder, M. J., R. K. Smith, J. R. Taylor, D. J. Low, S. J. Arnup, L. Muir, and G. Thomsen, 2013: Diurnally forced convergence lines in the australian tropics. *Q. J. R. Meteorol. Soc.*, **139**, 1283–1297, doi:10.1002/qj.2021.

Rife, D. L., J. O. Pinto, A. J. Monaghan, C. A. Davis, and J. R. Hannan, 2010: Global distribution and characteristics of diurnally varying low-level jets. *J. Clim.*, **23**, 5041–5064, doi:10.1175/2010JCLI3514.1.

Rogerson, A. M., 1999: Transcritical Flows in the Coastal Marine Atmospheric Boundary

Layer*. *J. Atmos. Sci.*, **56**, 2761–2779, doi:10.1175/1520-0469(1999)056<2761:TFITCM>2.0.CO;2.

Rojas, G. M., 2008: Low level jets in the tropical americas. Colorado State University, .

Rueda, C., 2015: Caracterización de la corriente en chorro de bajo nivel de los llanos orientales colombianos (Characterization of the low-level jet over the Colombian Eastern llanos),. Universidad Nacional de Colombia, 84 pp.

Rueda, O., and G. Poveda, 2006: Variabilidad espacial y temporal del chorro del "Chocó" y su efecto en la hidroclimatología de la región del pacífico colombiano. *Meteorol. Col*, 132–145.

Samelson, R. M., 1992: Supercritical Marine-Layer Flow along a Smoothly Varying Coastline. *J. Atmos. Sci.*, **49**, 1571–1584, doi:10.1175/1520-0469(1992)049<1571:SMLFAA>2.0.CO;2.

Shapiro, A., E. Fedorovich, and S. Rahimi, 2016: A Unified Theory for the Great Plains Nocturnal Low-Level Jet. *J. Atmos. Sci.*, **73**, 3037–3057, doi:10.1175/JAS-D-15-0307.1. http://journals.ametsoc.org/doi/10.1175/JAS-D-15-0307.1.

Silva, G. A. M., T. Ambrizzi, and J. A. Marengo, 2009: Observational evidences on the modulation of the South American Low Level Jet east of the Andes according the ENSO variability. *Ann. Geophys*, **27**, 645–657, doi:10.5194/angeo-27-645-2009. www.ann-geophys.net/27/645/2009/.

Simpson, J. E., 1987: *Gravity currents: in the environment and the laboratory*. Ellies Horwood Limited, Chichester, West Susex, England, 244 pp.

——, 1994: *Sea breeze and local winds*. Cambridge University Press, Cambridge, 234 pp.

Skamarock, W. C., and J. B. Klemp, 2008: A time-split nonhydrostatic atmospheric model for weather research and forecasting applications. *J. Comput. Phys.*, **227**, 3465–3485, doi:10.1016/j.jcp.2007.01.037.

Smith, R. K., G. Roff, and N. Crook, 1982: The Morning Glory: An extraordinary atmospheric undular bore. *Q. J. R. Meteorol. Soc.*, **8**, 937–956, doi:10.1002/qj.49710845813.

Soares, P. M. M., R. M. Cardoso, Á. Semedo, M. J. Chinita, and R. Ranjha, 2014: Climatology of the Iberia coastal low-level wind jet: Weather research forecasting model high-resolution results. *Tellus, Ser. A Dyn. Meteorol. Oceanogr.*, **66**, 1–19, doi:10.3402/tellusa.v66.22377.

Söderberg, S., and M. Tjernström, 2001: Supercritical channel flow in the coastal atmospheric boundary layer: Idealized numerical simulations. *J. Geophys. Res. Atmos.*, **106**, 17811–17829, doi:10.1029/2001JD900195. http://doi.wiley.com /10.1029/2001JD900195 (Accessed July 16, 2018).

Song, J., K. E. Liao, R. L. Coulter, and B. M. Lesht, 2005: Climatology of the Low-Level Jet at the Southern Great Plains Atmospheric Boundary Layer Experiments Site. *J. Appl. Meteorol.*, **44**, 1593–1606, doi:10.1175/JAM2294.1.

Squitieri, B. J., 2014: WRF forecast skill of the Great Plains low level jet and its correlation to forecast skill of mesoscale convective system precipitation. Iowa State University, 91 pp.

Stensrud, D. J., 1996: Importance of low-level jets to climate: A review. *J. Clim.*, **9**, 1698–1711, doi:10.1175/1520-0442(1996)009<1698:IOLLJT>2.0.CO;2.

Storm, B., J. Dudhia, S. Basu, A. Swift, and I. Giammanco, 2009: Evaluation of the weather research and forecasting model on forecasting low-level jets: Implications for wind energy. *Wind Energy*, **12**, 81–90, doi:10.1002/we.288.

Stull, R., 2015a: Atmospheric Boundary Layer. *Practical Meteorology: An algebra-based* *survey of atmospheric science*, University of British Columbia, Vancouver, BC, Canada, 687–722.

——, 2015b: Regional Winds. *Practical Meteorology: An algebra-based survey of atmospheric science*, University of British Columbia, Vancouver, BC, Canada, 645–686.

Taylor, J. R., 1997: *An introduction to error analysis: The study of uncertainties in physical measurements*. 2nd Edition. University Science Books, Sausalito, California, 327 pp.

Thompson, G., P. R. Field, R. M. Rasmussen, and W. D. Hall, 2008: Explicit Forecasts of Winter Precipitation Using an Improved Bulk Microphysics Scheme. Part II: Implementation of a New Snow Parameterization. *Mon. Weather Rev.*, **136**, 5095–5115, doi:10.1175/2008MWR2387.1. http://journals.ametsoc.org/doi/abs/10.1175/2008MWR2387.1.

Tim, N., and L. Bravo de Guenni, 2016: Oceanic influence on the precipitation in Venezuela under current and future climate. *Clim. Dyn.*, **47**, 211–234, doi:10.1007/s00382-015-2832-6.

Torrealba, E. R., and J. A. Amador, 2010: La corriente en chorro de bajo nivel sobre los Llanos Venezolanos de Sur América. *Rev. Climatol.*, **10**, 1–10.

Tripaldi, A., and M. A. Zárate, 2016: A review of Late Quaternary inland dune systems of South America east of the Andes. *Quat. Int.*, **410**, 96–110, doi:10.1016/j.quaint.2014.06.069.

Tsai, V. C., H. Kanamori, and J. Artru, 2004: The morning glory wave of southern California. *J. Geophys. Res*, **109**, 1–11, doi:10.1029/2003JB002596.

Unidad Administrativa de Aeronáutica Civil, 2017: Boletín Estadístico Diciembre 2017-Tráfico de Aeropuertos. http://www.aerocivil.gov.co/atencion/estadisticas-de-las-actividades-aeronauticas/_layouts/15/WopiFrame.aspx?sourcedoc=/atencion /estadisticas-de-las-actividades-aeronauticas/Estadsticas operacionales/Estadisticas Trafico de Aeropuertos Diciembre 2017.xls& (Accessed July 22, 2018).

Unidata/University Corporation for Atmospheric Research, National Centers for Environmental Prediction/National Weather Service/NOAA/U.S. Department of Commerce, and European Centre for Medium-Range Weather Forecasts, 2003: Historical Unidata Internet Data Distribution (IDD) Gridded Model Data. http://rda.ucar.edu/datasets/ds335.0/.

Vera, C., and Coauthors, 2006: The South American low-level jet experiment. *Bull. Am. Meteorol. Soc.*, **87**, 63–77, doi:10.1175/BAMS-87-1-63.

Vernekar, A. D., B. P. Kirtman, and M. J. Fennessy, 2003: Low-level jets and their effects on the South American summer climate as simulated by the NCEP Eta Model. *J. Clim.*, **16**, 297–311, doi:10.1175/1520-0442(2003)016<0297:LLJATE>2.0.CO;2.

Virji, H., 1981: A Preliminary Study of Summertime Tropospheric Circulation Patterns over South America Estimated from Cloud Winds. *Mon Weather Rev*, **109**, 599–610, doi:10.1175/1520-0493(1981)109<0599:APSOST>2.0.CO;2.

Walters, K., A. Korik, and M. J. Vojtesak, 1989: *The Caribbean basin: A climatological study*. USAF Environmental Technical Applications Center, Scott Air Force Base, Illinois, 342 pp.

Wang, H., R. Fu, J. K. Schemm, W. Tang, and W. T. Liu, 2008: Predictability of South American low-level jet using QuikSCAT ocean surface wind. *Int. J. Remote Sens.*, **29**, 6117–6127, doi:10.1080/01431160802175512.

Watson, C. D., and T. P. Lane, 2016: A Case of an Undular Bore and Prefrontal Precipitation in the Australian Alps. 2623–2644, doi:10.1175/MWR-D-15-0355.1.

Weaver, S. J., and S. Nigam, 2008: Variability of the great plains low-level jet: Large-scale circulation context and hydroclimate impacts. *J. Clim.*, **21**, 1532–1551, doi:10.1175/2007JCLI1586.1. http://journals.ametsoc.org/doi/abs/10.1175/2007JCLI1586.1 (Accessed July 16, 2018).

Wei, W., B. G. Wu, X. X. Ye, H. X. Wang, and H. S. Zhang, 2013: Characteristics and Mechanisms of Low-Level Jets in the Yangtze River Delta of China. *Boundary-Layer Meteorol.*, **149**, 403–424, doi:10.1007/s10546-013-9852-8.

Wexler, H., 1961: A Boundary Layer Interpretation of the Low-level Jet. *Tellus*, **13**, 368–378, doi:10.1111/j.2153-3490.1961.tb00098.x. http://tellusa.net/index.php/tellusa/article/view/9513.

Whiteman, C. D., X. Bian, and S. Zhong, 1997: Low-Level Jet Climatology from Enhanced Rawinsonde Observations at a Site in the Southern Great Plains. 1363–1376.

Whyte, F. S., M. A. Taylor, T. S. Stephenson, and J. D. Campbell, 2008: Features of the Caribbean low level jet. *Int. J. Climatol.*, **28**, 119–128, doi:10.1002/joc.1510. http://doi.wiley.com/10.1002/joc.1510 (Accessed July 16, 2018).

Van de Wiel, B. J. H., A. F. Moene, G. J. Steeneveld, P. Baas, F. C. Bosveld, and A. A. M. Holtslag, 2010: A Conceptual View on Inertial Oscillations and Nocturnal Low-Level Jets. *J. Atmos. Sci.*, **67**, 2679–2689, doi:10.1175/2010JAS3289.1. http://journals.ametsoc.org/doi/abs/10.1175/2010JAS3289.1.

Winant, C. D., C. E. Dorman, C. A. Friehe, and R. C. Beardsley, 1988: The marine layer off Northern California: an example of supercritical channel flow. *J. Atmos. Sci.*, **45**, 3588–3605, doi:10.1175/1520-0469(1988)045<3588:TMLONC>2.0.CO;2. papers2://publication/uuid/7501E73F-5524-4A5F-B5B5-818BDDBF3D8A.

Wolter, K., and M. S. M. S. Timlin, 1993: Monitoring ENSO in COADS with a seasonally adjusted principal component index. *Proceedings of the 17th Climate Diagnostics Workshop,* Norman, OK, NOAA/NMC/CAC, NSSL, Oklahoma Climate Survey, CIMMS and the School of Meteorology, University of Oklahoma, 52–57.

Wu, Y., and S. Raman, 1993: The Great Plains Low-Level Jet (LLJ) During the Atmospheric Radiation Measurement (ARM) Intensive Observation Period (IOP) -4 and Simulations of Land Use Pattern Effect on the LLJ Simulations of Land Use Pattern Effect on the LLJ Model Description. 367–371.

Young, G., and N. Winstead, 2005: Meteorological phenomena in high resolution SAR wind imagery. *High resolution wind monitoring with wide swath SAR: A user's guide*, National Oceanic and Atmospheric Administration, Washington DC, USA, 13–32.

Zhao, P., J. Sun, and X. Zhou, 2003: Mechanism of formation of low level jets in the South China Sea during spring and summer of 1998. *Chinese Sci. Bull.*, **48**, 1265–1270.

VITA

JORGE GIOVANNI JIMÉNEZ SÁNCHEZ

Email: jgj118@psu.edu

EDUCATION

2018 Ph.D. in Meteorology and Atmospheric Science
The Pennsylvania State University, University Park, PA

2004 Master of Science in Meteorology
Universidad Nacional de Colombia, Bogotá, Colombia

1999 Air Traffic Control-Aerodrome License
Unidad Administrativa Especial de Aeronáutica Civil, Bogotá, Colombia

1998 Bachelor of Aviation Business Administration
Escuela Militar de Aviación "Marco Fidel Suárez", Cali, Colombia

EXPERIENCE

The Pennsylvania State University

Poster presenter (17th Conference on Mesoscale Processes)	2017
Mesoscale meteorology teaching assistant	2016

Colombian Air Force

Director of Meteorology	2011-2014
Operational Weather Center Commander	2009-2012
Meteorology Instructor	2007-2014
Aerial Navigation Squadron Commander	2001-2006
German Olano aerodrome Control Tower Commander	2000

HONORS AND AWARDS

Chi Epsilon Pi - National Meteorology Honors Society member (U.S.A.)	2017
Colombian Air Force Cross - Aeronautical merit	2013
Military Medal "Marco Fidel Suárez"	2013
Instituto Militar Aeronáutico Distinguished Graduate	2011
Fellowship at the Tropical Desk of the National Centers for Environmental Prediction (NOAA-NCEP). Camp Springs – Maryland (U.S.A.)	2009
Science and Technology Award -Team	2007